

# Global and diurnal variations in tropospheric ammonia observed from a constellation of hyperspectral infrared sounders in three different LEO orbits

5 Jiancong Hua<sup>1</sup>, Runyi Zhou<sup>1</sup>, Mengya Sheng<sup>1</sup>, Zhao-Cheng Zeng<sup>1</sup>

<sup>1</sup>School of Earth and Space Sciences, Peking University, Beijing 100087, China

*Correspondence to: Zhao-Cheng Zeng (zczeng@pku.edu.cn)*

Abstract. As a reactive nitrogen compound, atmospheric ammonia (NH<sub>3</sub>) plays a key role in the global nitrogen cycle. Tracking the spatiotemporal dynamics of NH<sub>3</sub> is essential for quantifying its emissions and deposition and for informing the regulation of anthropogenic emission sources. Currently, the diurnal cycle of NH<sub>3</sub> remains under-constrained, particularly in regions lacking geostationary satellite observations, which poses a challenge to accurate emission quantification. To address this gap, we construct an integrated constellation to achieve quasi-geostationary-like global monitoring coverage, comprising China's FengYun-3 (FY-3) series satellites and the Cross-track Infrared Sounder (CrIS). FY-3E operates in a dawn-dusk orbit with an equatorial overpass time of 05:30 am/pm, while FY-3F operates in a mid-morning orbit with an overpass time of 10:00 am/pm. Both satellites are equipped with the second-generation High Spectral Infrared Atmospheric Sounder (HIRAS-II). CrIS, with an overpass time of 01:30 am/pm, provides supplementary observations in an afternoon orbit. In this study, hyperspectral infrared observations from the constellation are utilized to retrieve global NH<sub>3</sub> columns based on the optimal estimation method. Six global NH<sub>3</sub> maps are retrieved per day at approximately 4-hour intervals. The retrieval results for four representative weeks in different seasons of 2024, as a demonstration, show elevated columns in major source regions, including the North China Plain, the Indo-Gangetic Plain, North America and Western Europe. In addition, the diurnal and seasonal cycles of NH<sub>3</sub> over these regions using all observations in 2024 are also investigated. The constellation captures the diurnal (every 4-hour) and seasonal cycles of NH<sub>3</sub> columns, effectively mitigating the constraints in regions without geostationary observations. Further cross-comparisons with the Geostationary Interferometric Infrared Sounder (GIIRS) retrievals and ground-based Fourier transform infrared spectroscopy (FTIR) measurements demonstrate that the polar-orbiting constellation retrievals are internally consistent and broadly consistent with independent observations, supporting their capability to capture major NH<sub>3</sub> spatial patterns and temporal variability. The sensitivity of NH<sub>3</sub> detection in the lower atmosphere, quantified by the column averaging kernel (AVK), exhibits diurnal variability linked to thermal contrast, defined as the temperature difference between the surface and the lowest atmospheric layer. This study demonstrates the capability of an integrated constellation comprising FY-3E/HIRAS-II in a dawn-dusk orbit, FY-3F/HIRAS-II in a mid-morning orbit, and CrIS in an afternoon orbit to monitor global NH<sub>3</sub> distributions and diurnal variability at an unprecedented six local times per day. This approach highlights the potential of polar-orbiting meteorological satellites to enhance the global climate monitoring.

## 1 Introduction

As a critical reactive nitrogen compound, ammonia ( $\text{NH}_3$ ) holds considerable importance in the atmosphere and global nitrogen cycle, yet it also acts as a hazardous pollutant affecting human health and ecosystems. Specifically, it contributes to smog via its neutralization of sulfuric and nitric acids, resulting in the generation of secondary aerosols including ammonium sulfate and ammonium nitrate (Galloway et al., 2004; Behera et al., 2013). These particles can travel long distances, degrading air quality and disrupting ecological balance (Erismann et al., 2013).  $\text{NH}_3$  and ammonium-containing particles participate in the cascade of reactive nitrogen transformations, with broad impacts on air, water, soil quality, climate, and biodiversity (Sutton et al., 2013). Under specific conditions, ammonium nitrate particles may volatilize to reform gaseous  $\text{NH}_3$ , creating a dynamic cycle that complicates its environmental impacts (Weber et al., 2016; Guo et al., 2018). Agriculture serves as the dominant source, stemming from fertilizer storage, livestock manure, and the application of mineral nitrogen fertilizers to crops (Fowler et al., 2013). Secondary contributors to  $\text{NH}_3$  emissions encompass biomass combustion, industrial operations, and automobiles fitted with three-way catalytic converters (Galloway et al., 2003; Erismann et al., 2008). After being emitted into the atmosphere,  $\text{NH}_3$  exhibits a brief residence time ranging from several hours to a handful of days, and its primary removal pathways are dry and wet deposition processes (Liu et al., 2013; Dammers et al., 2017; Zhang et al., 2018). These deposition processes accelerate soil acidification, further exacerbating the ecological damage. Beyond air quality and ecosystem impacts, the aerosols derived from  $\text{NH}_3$  also influence climate by scattering solar radiation, modifying albedo, and altering the properties of clouds (Adams et al., 2001; Abbatt et al., 2006; Isaksen et al., 2009; Myhre et al., 2013).

Different technologies have been used to monitor atmospheric  $\text{NH}_3$ . A number of in situ monitoring sites have been established (Jiménez et al., 2015; De Mazière et al., 2018). Moreover, satellites equipped with high-resolution infrared spectrometers have provided unprecedented spatiotemporal sampling of global  $\text{NH}_3$  distributions, and this has driven major progress in understanding  $\text{NH}_3$  emission and deposition fluxes covering spatial scales ranging from local to global, together with their temporal variability. Polar-orbiting satellites are capable of delivering global observational coverage up to two times per day, including the Infrared Atmospheric Sounding Interferometers (IASI, e.g., Clarisse et al., 2009) at 09:30/21:30 (Local Solar Time, LST), Tropospheric Emission Spectrometer (TES, e.g., Beer et al., 2008; Shephard et al., 2011), the Atmospheric Infrared Sounder (AIRS, e.g., Warner et al., 2016) and the Cross-track Infrared Sounder (CrIS, e.g., Shephard and Cady-Pereira, 2015) at 01:30/13:30 LST, the Thermal and Near-infrared Spectrometer for Observation-Fourier Transform Spectrometer (TANSO-FTS; e.g., Someya et al., 2020) at 01:00/13:00 LST and FengYun-3D (FY-3D, e.g. Zhou et al., 2024) at 02:00/14:00 LST. Recently, diurnal variations of atmospheric  $\text{NH}_3$  over the Asian region have been observed using the Geostationary Interferometric Infrared Sounder (GIIRS) aboard the FengYun-4A (FY-4A/GIIRS, Clarisse et al., 2021) and FengYun-4B (FY-4B/GIIRS, (Zeng et al., 2023; Sheng et al., 2026; Guendouz et al., 2026) satellites. The Infrared Sounder (IRS) aboard the Meteosat Third Generation (MTG), which was launched in 2025, is expected to provide geostationary observations over Europe and Africa (Holmlund et al., 2021; Guendouz et al., 2026). Such geostationary orbit-based monitoring offers significant advantages and potential for investigating  $\text{NH}_3$  diurnal variations, which in turn facilitates a

65 deeper understanding of its emission, deposition, transport and other related processes. However, there is currently a lack of geostationary orbit observations across most global regions, especially much of the Southern Hemisphere and North America. Atmospheric  $\text{NH}_3$  shows notable spatiotemporal variability, largely attributed to its primary emission characteristics and short atmospheric lifetime. This inherent variability underscores the urgent need for a high-resolution and globally comprehensive monitoring system.

70 To address this gap, we construct an integrated constellation to achieve quasi-geostationary-like global monitoring coverage, comprising China's FengYun-3 (FY-3) series satellites and CrIS. A similar constellation has been developed for monitoring volcanic sulfur dioxide (Zeng et al., 2025).  $\text{NH}_3$  retrievals based on the optimal estimation method are conducted under this framework to enable quasi-geostationary-like observations up to six times per day globally. This work is expected to provide crucial observational data for clarifying global and diurnal  $\text{NH}_3$  variations.

75 The subsequent sections of this paper are organized as follows. Section 2 elaborates on the methodological approaches adopted in the present research. Section 3 presents and discusses the retrieval results from the constellation. Finally, the conclusions are drawn in Section 4.

## 2 Methodologies

### 2.1 A constellation of hyperspectral infrared sounders

80 The High Spectral Infrared Atmospheric Sounder (HIRAS) aboard the FY-3 satellite series is a Fourier Transform Michelson interferometer. It measures upwelling infrared radiative signals across the short-wave, mid-wave, and long-wave infrared bands. HIRAS-II is the second generation of the HIRAS sensor and is carried onboard both FY-3E and FY-3F, which were successfully launched in 2021 and 2023, respectively (Zhang et al., 2022a, b). FY-3E/HIRAS-II is deployed in a dawn-dusk orbit, with an equatorial overpass time of 05:30 am/pm LST, while FY-3F/HIRAS-II operates in a mid-morning orbit  
85 featuring an overpass time of 10:00 am/pm LST. Combined with CrIS aboard the Joint Polar Satellite System-1 (JPSS-1) platform, which has an overpass time of 01:30 am/pm LST, these three sensors form a global constellation observation system (Fig. 1a). Note that IASI's overpass times, approximately 09:30 and 21:30 LST, are close to those of FY-3F/HIRAS-II at 10:00 and 22:00 LST and thus can provide additional mid-morning orbit observations. For this concept study, however, only FY-3F/HIRAS-II is used. Their overpass times are shown in Fig. 1b, and the corresponding histograms are presented in Fig. 1c.

90 Both HIRAS-II instruments aboard the FY-3E and FY-3F satellites, together with CrIS, share key technical specifications with a nadir spatial resolution of 14 km and an unapodised spectral resolution of  $0.625 \text{ cm}^{-1}$  (Zhang et al., 2024). Specifically, HIRAS-II provides continuous spectral coverage across  $650\text{--}2550 \text{ cm}^{-1}$  via 3041 channels, while CrIS matches this spectral resolution, ensuring all three instruments fully cover the characteristic rotational-vibrational  $\nu_2$  band of  $\text{NH}_3$  centered near  $10.5 \mu\text{m}$ . For  $\text{NH}_3$  retrieval, we use the  $955\text{--}975 \text{ cm}^{-1}$  band extracted from observations of all three instruments.  
95 No empirical sensor-specific radiometric bias correction or additional spectral harmonization is applied before the retrievals. We randomly select one day of observations from the three satellites over the North China Plain and estimate their spectral

noise. The noise equivalent differential temperature (NedT) of HIRAS-II aboard FY-3E and FY-3F is approximately 0.08 K, while that of CrIS is around 0.05 K. These noise levels are of a comparable magnitude and sufficiently sensitive to detect variations in NH<sub>3</sub>, ensuring uniform observational quality for cross-instrument analysis (Zavyalov et al., 2013; Shephard and Cady-Pereira, 2015; Zhang et al., 2024). While CrIS already has well-established and mature NH<sub>3</sub> products from the CrIS Fast Physical Retrieval (CFPR) dataset developed by Environment and Climate Change Canada (Shephard et al., 2020), we adopt a unified retrieval algorithm for all three instruments. This choice is driven by the need to ensure consistency across the satellite constellation, enabling direct inter-comparability between FY-3E/HIRAS-II, FY-3F/HIRAS-II, and CrIS observations. For CrIS retrievals, we use JPSS-1 CrIS Level 1B Full Spectral Resolution V3 data as input, maintaining methodological coherence with our processing of HIRAS-II observations.

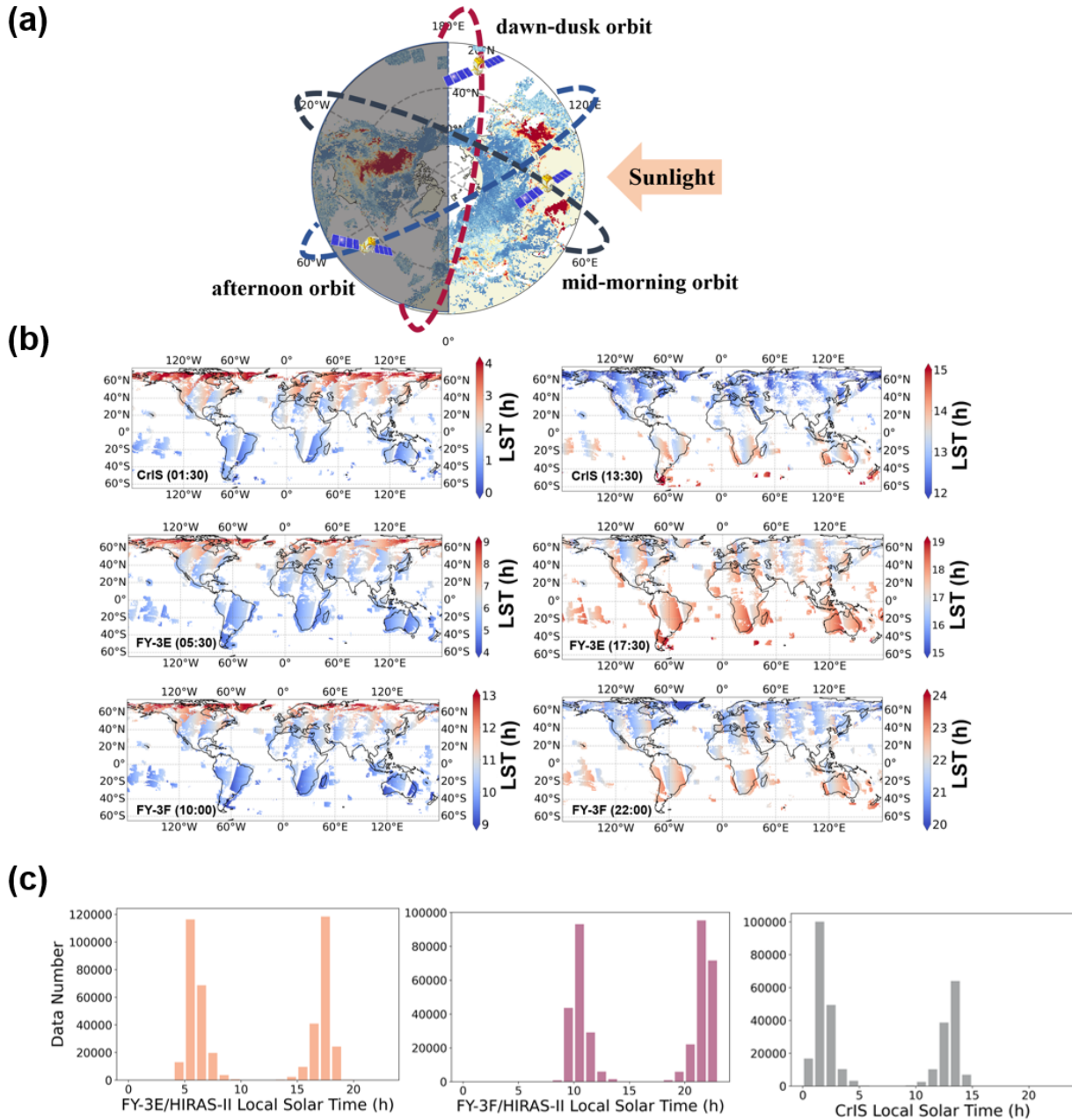


Figure 1. (a) Schematic diagram of three polar-orbiting satellites with different orbits. FY-3E/HIRAS-II operates in a dawn-dusk orbit, with an equatorial overpass time of 05:30 am/pm LST, FY-3F/HIRAS-II is in a mid-morning orbit with an equatorial overpass time of 10:00 am/pm LST, and the CrIS has an equatorial overpass time of 01:30 am/pm LST. The color gradient in the background represents the retrieved global distribution of  $\text{NH}_3$  columns on 19 July 2024, as will be discussed in subsequent analyses. (b) LST of observations acquired by FY-3E/HIRAS-II, FY-3F/HIRAS-II and CrIS over terrestrial and offshore regions. Observations over polar areas and remote oceans are excluded. These maps are constructed from cloud-screened observations collected on 19 July, 2024. (c) Histograms of the overpass LST for FY-3E/HIRAS-II, FY-3F/HIRAS-II, and CrIS. Examples are derived from observations taken on 19 July, 2024.

## 2.2 Optimal estimation methods

For the retrieval, only cloud-screened spectra from FY-3E/HIRAS-II, FY-3F/HIRAS-II, and CrIS are used. To remove cloud-contaminated pixels and ensure consistency across sensors, we apply a unified cloud-screening procedure following the brightness-temperature-difference method of Wells et al. (2020, 2022). Specifically, for each observation, the observed brightness temperature near  $900\text{ cm}^{-1}$  is compared with the nearest-hourly surface skin temperature obtained from European Centre for Medium-Range Weather Forecasts (ECMWF) Reanalysis v5 (ERA5). The cloud-screening threshold is adjusted according to the ERA5 water vapor column, and no fixed cloud-fraction threshold is used. Observations for which the  $900\text{ cm}^{-1}$  brightness temperature is lower than this water-vapor-dependent threshold relative to the surface skin temperature are flagged as cloud-contaminated and excluded. The same cloud-screening procedure is applied to FY-3E/HIRAS-II, FY-3F/HIRAS-II, and CrIS to maintain consistency across different satellites.

The  $\text{NH}_3$  retrieval is based on the FengYun-Low Earth Orbit Atmospheric Infrared Retrieval algorithm (FY-LeoAIR), which adapts the optimal-estimation framework and forward-model structure of the FY-GeoAIR algorithm originally developed for FY-4B/GIIRS  $\text{NH}_3$  retrievals by Zeng et al. (2023). FY-LeoAIR has previously been applied to trace gas retrievals from FY-3E/HIRAS-II observations, including CO and VOCs (e.g., Zeng, 2025; Hua et al., 2025). In this study, FY-LeoAIR is extended to global  $\text{NH}_3$  retrievals from FY-3E/HIRAS-II, FY-3F/HIRAS-II, and CrIS.

The retrieval is performed in the  $955\text{--}975\text{ cm}^{-1}$  band, which contains strong  $\text{NH}_3$  absorption features and is fully covered by all three sensors. Sensor-specific spectral noise estimates are used to construct the diagonal measurement-error covariance matrix. The same forward model, retrieval method, and quality-control procedure are used for all three sensors to maintain internal consistency.

FY-LeoAIR combines a clear-sky infrared radiative transfer forward model with an optimal-estimation-based inverse model. The forward model uses atmospheric temperature, water vapor ( $\text{H}_2\text{O}$ ), ozone ( $\text{O}_3$ ), and surface pressure from ERA5,  $\text{CO}_2$  from ECMWF Copernicus Atmosphere Monitoring Service (CAMS) greenhouse-gas products, and other weakly interfering trace-gas profiles from standard atmospheric profiles, following the configuration of Zeng et al. (2023). Surface skin temperature is initialized from ERA5 and retrieved simultaneously with the trace gases. The a priori land surface emissivity used in the forward model is obtained from the University of Wisconsin-Madison global infrared land surface emissivity database (UOW-M), as in Zeng et al. (2023). It is adjusted within the retrieval window using a multiplicative Legendre polynomial expansion, in which the zeroth-order term is fixed to unity and four coefficients corresponding to the first- to fourth-order terms are retrieved simultaneously. The parameters in the retrieval state vector are summarized in Table S1.

The main modification relative to Zeng et al. (2023) is that  $\text{NH}_3$  is retrieved using a single multiplicative profile-scaling factor applied to a fixed a priori  $\text{NH}_3$  profile, rather than as independent layer-by-layer  $\text{NH}_3$  elements. The same profile-scaling strategy is also applied to  $\text{H}_2\text{O}$  in this implementation. This approach is adopted because the  $\text{NH}_3$  information content

in individual thermal infrared observations is generally limited, with the degree of freedom for signal mostly below 1, making independent layer-resolved retrievals insufficiently constrained for global multi-sensor processing. The profile-scaling approach also improves computational efficiency for the global constellation retrieval. A similar retrieval strategy has also been adopted by FY-4B/GIIRS NH<sub>3</sub> retrievals (Sheng et al., 2026).

The fixed NH<sub>3</sub> a priori profile is constructed following Zeng et al. (2023), based on Goddard Earth Observing System composition forecast (GEOS-CF) NH<sub>3</sub> simulations over representative polluted land regions in East Asia and South Asia. The same normalized profile shape is used for all retrievals, while the retrieved scaling factor determines the retrieved NH<sub>3</sub> abundance. This choice helps avoid introducing artificial spatial or temporal variability from a time-varying prior into the retrieved columns. Retrieval uncertainty and the column averaging kernel are used to characterize the information content of each retrieval. We also conduct an a priori profile sensitivity test (see Text S1 and Figs. S1–S6 in the supplementary material).

Because NH<sub>3</sub> is mainly concentrated in the lower troposphere, the retrieval state vector only adjusts NH<sub>3</sub> in 11 atmospheric layers from the surface to 200 hPa. The reported NH<sub>3</sub> total column is calculated as the sum of the retrieved surface-to-200 hPa NH<sub>3</sub> column and the fixed a priori contribution above 200 hPa. Since the NH<sub>3</sub> abundance above 200 hPa is generally small and is not independently constrained by the spectra, the spatial and temporal variability discussed in this study is dominated by the retrieved surface-to-200 hPa component.

An optimal state vector for minimizing discrepancies between forward model-simulated spectra and sensor-measured spectra is derived by the optimal estimation framework. In practice, the retrieval algorithm outputs the state vector that minimizes the cost function defined as:

$$J(\mathbf{x}) = \chi^2 = [\mathbf{y} - \mathbf{F}(\mathbf{x}, \mathbf{b})]^T \mathbf{S}_\epsilon^{-1} [\mathbf{y} - \mathbf{F}(\mathbf{x}, \mathbf{b})] + (\mathbf{x} - \mathbf{x}_a)^T \mathbf{S}_a^{-1} (\mathbf{x} - \mathbf{x}_a), \quad (1)$$

Here,  $\mathbf{y}$  denotes the satellite-measured radiance within the NH<sub>3</sub> retrieval band.  $\mathbf{F}$  is the forward model that produces simulated radiance for the retrieval process.  $\mathbf{x}$  is the retrieval state vector, including the NH<sub>3</sub> profile-scaling factor, the H<sub>2</sub>O profile-scaling factor, scaling factors for interfering trace gases, surface skin temperature, atmospheric temperature scaling, and four surface-emissivity Legendre polynomial coefficients.  $\mathbf{x}_a$  denotes the a priori vector.  $\mathbf{b}$  stands for a set of fixed non-retrieved auxiliary parameters.  $\mathbf{S}_a$  is the a priori covariance matrix corresponding to the state vector.  $\mathbf{S}_\epsilon$  represents the measurement error covariance matrix, treated as a diagonal matrix derived from spectral noise estimates. Retrieval outputs include the NH<sub>3</sub> column, posteriori column retrieval uncertainty estimation, and column averaging kernel (AVK). The column AVK quantitatively represents the response of total NH<sub>3</sub> column to variations in the partial column at each layer, which is important for cross-comparison and model assimilation of satellite retrievals. A more detailed description of column AVK is provided in Sheng et al. (2026).

### 3 Results and Discussions

#### 3.1 Global variations of NH<sub>3</sub> columns from the LEO constellation

As an illustrative demonstration of the global sampling capability of the LEO constellation, we first examine  
180 representative seven-day mean NH<sub>3</sub> column distributions in January, April, July, and October 2024, specifically January 12–  
18, April 12–18, July 17–23, and October 1–7. These weekly maps are intended to demonstrate the global spatial coverage  
and broad seasonal contrast captured by the constellation, rather than to provide a climatological seasonal mean. We first  
retrieve global daily maps of NH<sub>3</sub> columns, re-grid them to a 0.5° × 0.5° spatial resolution, and then calculate seven-day  
averages for these representative periods. A quality control process is applied to ensure the reliability of satellite retrievals.  
185 Observations that fail to achieve convergence within 10 iterations are excluded from the dataset. We then implement a series  
of post-filters, retaining only those retrieval results that satisfy all the following criteria simultaneously. First, the retrieved  
NH<sub>3</sub> columns are required to be positive. Second, the absolute difference in surface skin temperature between the a priori and  
retrieved values is less than 10 K. Third, the retrieval error of the column does not exceed 300%. Fourth, the surface AVK is  
greater than 0.1. Fifth, the absolute thermal contrast (TC), defined as the temperature difference between the surface and the  
190 lowest atmospheric layer, is larger than 3 K. The absolute TC > 3 K and surface AVK > 0.1 criteria used here are intended for  
the global spatial-distribution analysis, where the objective is to illustrate the broad coverage and spatial patterns retrieved by  
the LEO constellation while retaining sufficient sampling density. These criteria remove retrievals with weak thermal contrast  
and limited near-surface sensitivity, but they are less restrictive than the criteria used later for the regional hotspot diurnal  
analysis. The effect of different TC and AVK thresholds on spatial distributions, diurnal cycles, and data retention is further  
195 evaluated and presented in the Supplementary Figs. S7–S10. Sixth, a threshold for surface emissivity at 8.3 μm is set at 0.9,  
with only results meeting this threshold retained. This step avoids abnormally high NH<sub>3</sub> column concentrations over desert  
regions, following the method of Clarisse et al. (2019). The surface emissivity data used for this filter are obtained from the  
Combined ASTER and MODIS Emissivity over Land Database Monthly Global 0.05° V003, which provides global monthly  
emissivity data at a 0.05° spatial resolution.

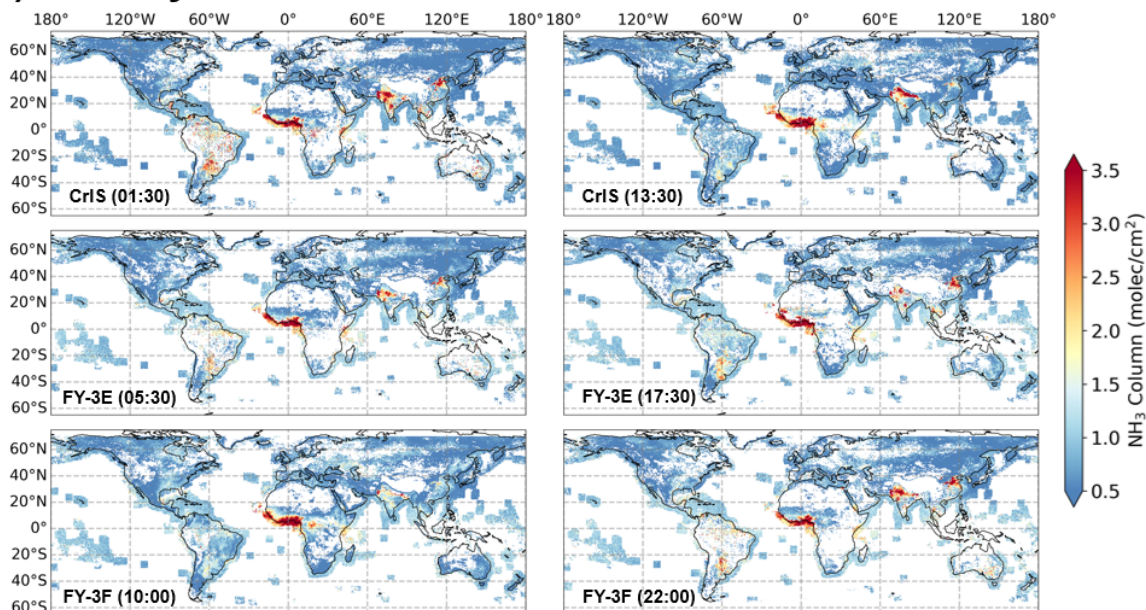
200 As shown in Figs. 2 and 3, broad seasonal contrasts in the representative weekly global NH<sub>3</sub> maps are evident across  
the four selected periods. In January, elevated NH<sub>3</sub> columns are concentrated in the Indo-Gangetic Plain and Central Africa,  
which is primarily associated with ongoing agricultural activities such as winter fertilizer application and extensive biomass  
burning for land clearance in these regions. In April, high NH<sub>3</sub> loading persists in the Indo-Gangetic Plain, East China and  
Central Africa, driven by intensified spring planting and corresponding fertilizer use in agricultural hotspots. Southeast Asia  
205 also exhibits increased NH<sub>3</sub> levels during this month, a pattern attributed to widespread slash-and-burn agriculture practices  
that are common in the regional dry season to prepare farmland. Additionally, scattered high NH<sub>3</sub> columns are observed in  
parts of North America, likely linked to localized agricultural operations and small-scale biomass burning. In July, high NH<sub>3</sub>  
columns remain concentrated in the Indo-Gangetic Plain, the North China Plain, Central Africa and Western Europe. The  
sustained high levels in these areas correlate with summer agricultural activities and elevated temperatures that enhance

210 emissions (Ding et al., 2024). In particular, large-scale wildfires during the summer in North America exert a broad regional  
impact, leading to significantly elevated  $\text{NH}_3$  columns across extensive regions as a result of biomass burning releasing  
substantial amounts of  $\text{NH}_3$  (Lutsch et al., 2019). Within smoke plumes, gas-phase  $\text{NH}_3$  can rapidly partition into particulate  
ammonium, especially in fresh, dense plumes injected into colder, higher-altitude air where ammonium nitrate formation is  
favored. Together with plume transport and dilution, this partitioning may modulate the observed  $\text{NH}_3$  columns as the smoke  
215 evolves (Lindaas et al., 2021). October still sees detectable high  $\text{NH}_3$  columns over the Indo-Gangetic Plain, where post-harvest  
agricultural residue burning and late-season fertilizer application maintain elevated emissions. In South America, elevated  $\text{NH}_3$   
levels are mostly attributed to combined effects of fertilizer usage for autumn crops and biomass burning, as documented by  
Luo et al. (2022). The seasonal patterns reflect the close linkage between  $\text{NH}_3$  distribution and region-specific anthropogenic  
activities, alongside seasonal natural processes. These spatial patterns exhibit general consistency with results from IASI (e.g.,  
220 Van Damme et al., 2015) and CrIS (e.g., Shephard et al., 2020).

We note that these weekly global maps may still be influenced by short-term episodic events, such as biomass burning.  
Therefore, they are used here primarily as representative examples of the constellation-derived global  $\text{NH}_3$  spatial distributions.  
The more quantitative regional diurnal and seasonal analyses in Section 3.2 are based on full-month averages using all available  
observations in each selected month.

225

### (a) January 12-18, 2024



### (b) April 12-18, 2024

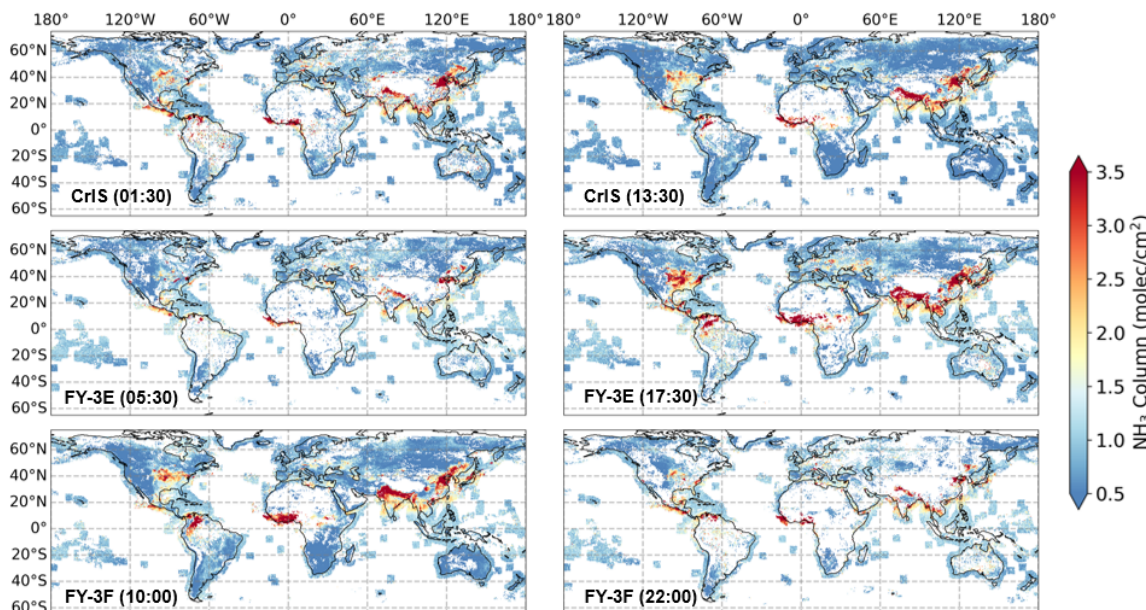
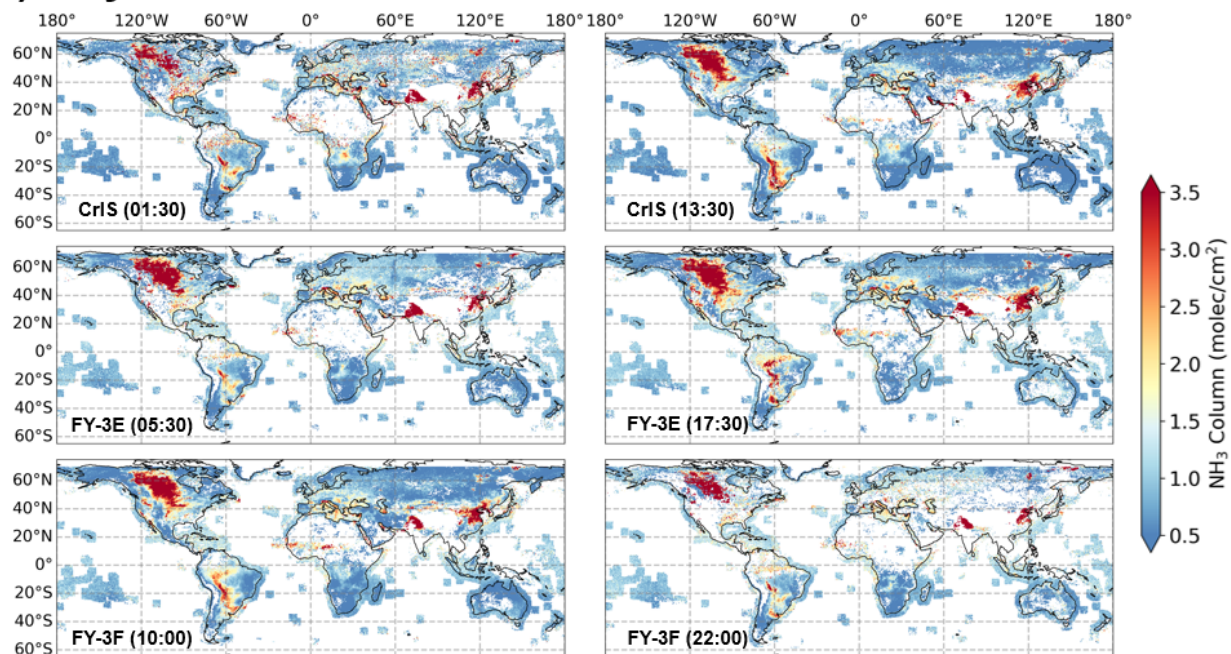


Figure 2. Representative seven-day mean  $\text{NH}_3$  columns retrieved from FY-3E, FY-3F, and CrIS for six different time slots, gridded to a  $0.5^\circ \times 0.5^\circ$  spatial resolution. The data correspond to the period of (a) January 12–18, 2024 and (b) April 12–18, 2024.

### (a) July 17-23, 2024



### (b) October 1-7, 2024

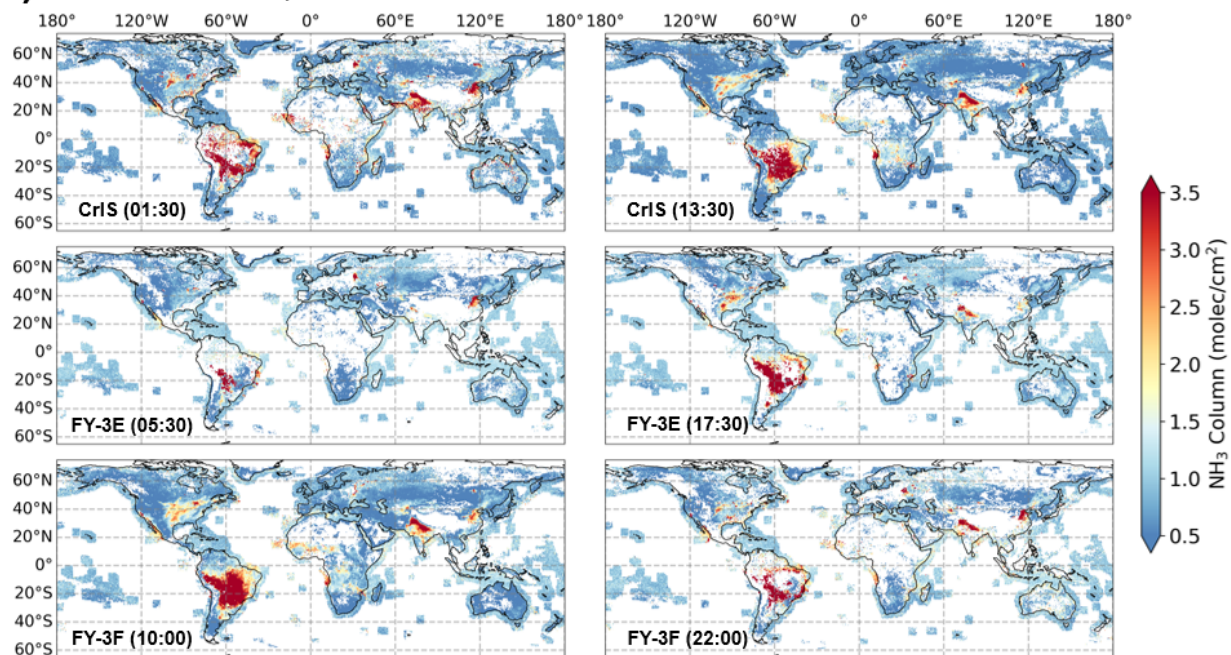


Figure 3. Same as Fig. 2, but for the period of (a) July 17–23, 2024 and (b) October 1–7, 2024.

### 3.2 NH<sub>3</sub> variations in major source regions from the LEO constellation

To conduct an in-depth analysis of NH<sub>3</sub> variations, we select three major emission hotspots located in the North China Plain (118°E, 37°N), the Indo-Gangetic Plain (78°E, 28°N), and the Central United States (100.5°W, 36.5°N), respectively. These hotspots are characterized by intensive agricultural activities and high livestock densities, consistent with the high-emission areas for their substantial NH<sub>3</sub> column abundances and distinct diurnal and seasonal dynamics. For each hotspot, we extract data within a 2.5° × 2.5° grid centered at the specified coordinates, covering six overpass times per day. A 2.5° × 2.5° box is selected to balance spatial representativeness and sample size. Because the analysis separates retrievals by satellite overpass time and month and further applies strict quality filters, a smaller box would often lead to insufficient valid retrievals, especially during nighttime or low-sensitivity conditions. The selected box size provides enough samples for stable monthly means while still focusing on the core NH<sub>3</sub> hotspot regions. The monthly mean is calculated only when the number of filtered retrievals within the 2.5° × 2.5° box exceeds 10 during that month. TC affects the retrieval accuracy (Bauduin et al., 2017), and higher absolute TC contributes to better retrievals (Clarisse et al., 2010). When TC is close to zero, the NH<sub>3</sub> spectral signal becomes weak and the retrieval sensitivity decreases, whereas a larger absolute TC generally enhances the spectral signal and improves the retrieval sensitivity. To ensure high-quality NH<sub>3</sub> column retrievals, we apply stricter sensitivity filters than those used for the global spatial-distribution maps in Section 3.1. Specifically, the same basic quality-control criteria are used, but the TC and AVK thresholds are tightened from absolute TC > 3 K and surface layer AVK value > 0.1 to absolute TC > 5 K and surface layer AVK value > 0.3. These stricter criteria are adopted to reduce the influence of local-time-dependent retrieval sensitivity on the inferred diurnal cycles, because TC itself has a pronounced diurnal variation.

The diurnal cycles of full-month averaged NH<sub>3</sub> columns for the three hotspots in each selected month are presented in Fig. 4, with the IASI NH<sub>3</sub> ANNI V4.0 product overlaid for comparison. Also shown are the monthly mean planetary boundary layer heights (BLH) from ERA5 reanalysis. All three hotspots exhibit consistent seasonal differences in diurnal variability, a pattern that is consistent with the findings of Clarisse et al. (2021) from GIRS observations and aligns with broader research on NH<sub>3</sub> dynamics (Tevlin et al., 2017). Warmer months (April–September) show distinct day-night contrasts, while winter months (December–February) display minimal diurnal fluctuations.

For the North China Plain (Fig. 4a), FY-3E, FY-3F, CrIS, and IASI data collectively reveal that warm-season NH<sub>3</sub> columns follow a clear diurnal pattern with a peak between 10:00 and 13:30 LST, and nighttime values approximately 50–60% lower than daytime maxima. The peak corresponds to intensified agricultural activities (e.g., fertilization and livestock management) and temperature-driven volatilization from soils and animal waste, mechanisms identified by Ernst and Massey (1960) and Sutton et al. (2013) as primary drivers of daytime NH<sub>3</sub> emission enhancement. Higher BLH during the day facilitates vertical diffusion of NH<sub>3</sub> and contributes to the observed column dynamics (Saylor et al., 2010). In contrast, winter NH<sub>3</sub> columns over the North China Plain show negligible diurnal variation, which is probably due to the fact that cold-season emissions are limited by low temperatures and reduced agricultural activity (Kuang et al., 2020; Clarisse et al., 2021).

The Indo-Gangetic Plain (Fig. 4b) exhibits the highest overall  $\text{NH}_3$  columns among the three hotspots, with warm-  
265 season daytime columns nearly double those of the North China Plain. The lower  $\text{NH}_3$  columns over the North China Plain  
relative to the Indo-Gangetic Plain may partly reflect higher levels of  $\text{NO}_x$  and  $\text{SO}_2$  (Clarisse et al., 2021; Ding et al., 2024),  
which can be oxidized to nitric and sulfuric acids and promote the conversion of gaseous  $\text{NH}_3$  to particulate ammonium,  
thereby shortening the effective lifetime of gas-phase  $\text{NH}_3$  (Liu et al., 2018; Wang et al., 2020). The most pronounced warm-  
season diurnal amplitude appears in the Indo-Gangetic Plain, with daytime columns up to three times higher than nighttime  
270 values. This pattern reflects the intensive irrigated agriculture and livestock-related emissions in the region, together with the  
strong temperature dependence of  $\text{NH}_3$  volatilization (Hempel et al., 2016; Perrone, 2020; Wang et al., 2020). Winter diurnal  
variations here are similarly weak, though  $\text{NH}_3$  columns remain higher than those in the other two regions due to persistent  
agricultural activity in milder winter conditions (Saraswati et al., 2018).

For the Central U.S. (Fig. 4c), the diurnal variation pattern is broadly consistent with the Asian regions but with a  
275 smaller amplitude. Warm-season  $\text{NH}_3$  columns peak between 11:00 and 14:00 LST, with daytime values approximately 1.5–  
2 times higher than nighttime levels, while winter columns show little diurnal fluctuation. This consistency supports the  
interpretation that temperature, BLH dynamics, and diurnally varying emissions (e.g., agricultural activities) are common  
drivers of  $\text{NH}_3$  diurnal cycles across major high-emission regions. This interpretation is consistent with the analysis of  $\text{NH}_3$   
measurements in the southeastern U.S. by Saylor et al. (2010). The smaller amplitude compared to the Indo-Gangetic Plain  
280 likely reflects moderate temperature variations and balanced  $\text{NH}_3$  emission and deposition processes, as reported by Warner  
et al. (2017) in satellite observations of North American agricultural regions. Li et al. (2026) further emphasize that local  
deposition in vegetation-dense areas offsets large-scale transport, explaining the muted diurnal amplitude relative to Asian  
regions.

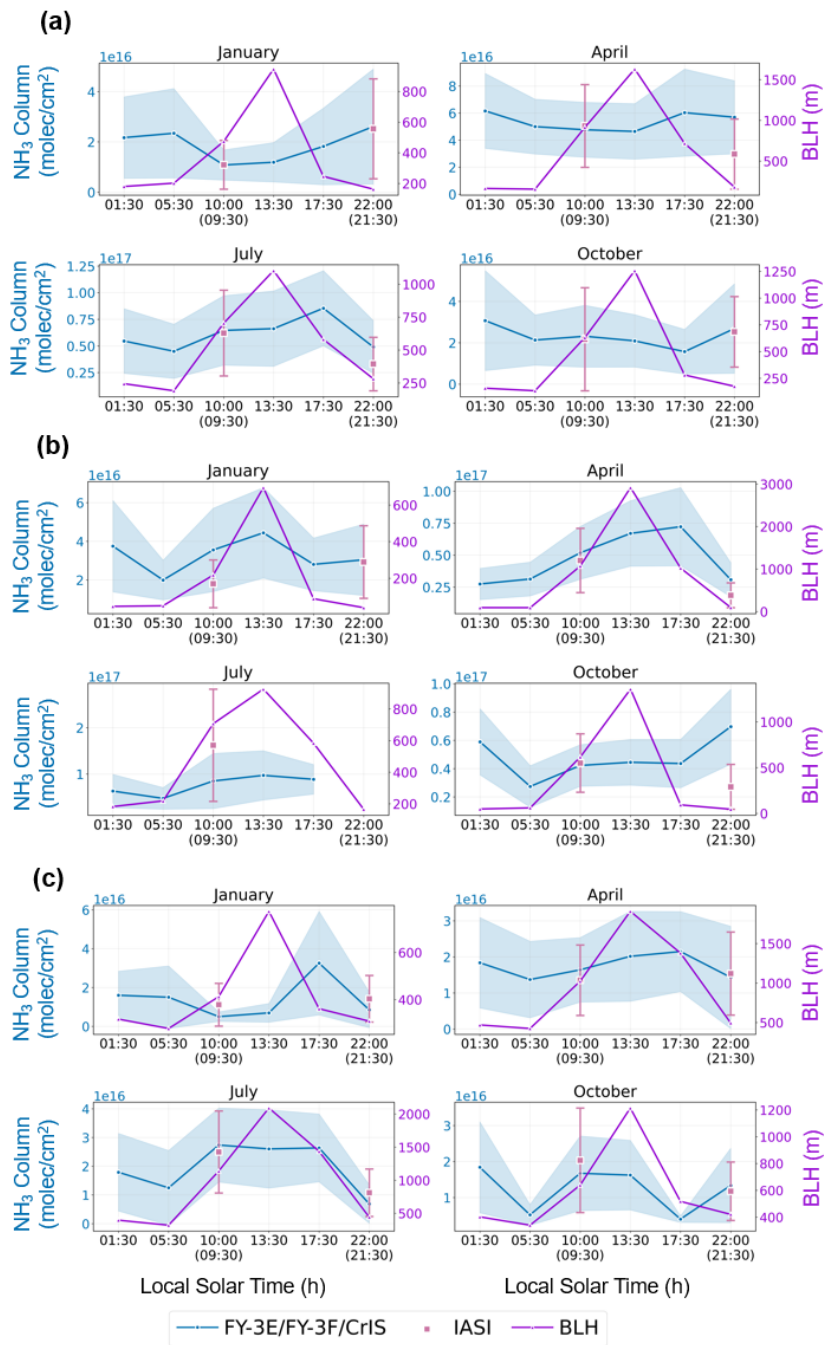
The spatial and seasonal dynamics of  $\text{NH}_3$  columns are further illustrated in Figs. 5–7 for the North China Plain, Indo-  
285 Gangetic Plain, Central U.S., respectively, retrieved from FY-3E/HIRAS-II, FY-3F/HIRAS-II and CrIS. Fig. A1 further  
illustrates monthly mean  $\text{NH}_3$  column variations for these three regions, confirming consistent time series across the six daily  
satellite overpasses and coherent seasonal trends. All three regions exhibit a consistent seasonal peak in  $\text{NH}_3$  columns during  
spring to summer (March–August), with the lowest values in winter (December–February). For the North China Plain (Fig. 5),  
all retrievals at six distinct times show that  $\text{NH}_3$  columns peak in June, with spatial coverage expanding across the entire plain  
290 during warm months, reflecting widespread agricultural activities (e.g., wheat fertilization and livestock waste management)  
and favorable meteorological conditions for emission (Zhang et al., 2010; Zhan et al., 2021). In contrast, winter maps display  
sparse, localized high- $\text{NH}_3$  patches, consistent with reduced agricultural activity and lower temperature-driven volatilization  
(Schjoerring et al., 1998).

For the Indo-Gangetic Plain, Fig. 6 shows that the region maintains the highest  $\text{NH}_3$  columns year-round, with spatial  
295 hotspots concentrated in the central plain during both day and night. However, daytime maps exhibit broader coverage  
extending to the plain's peripheries, while nighttime maps show more concentrated hotspots near emission sources. For the

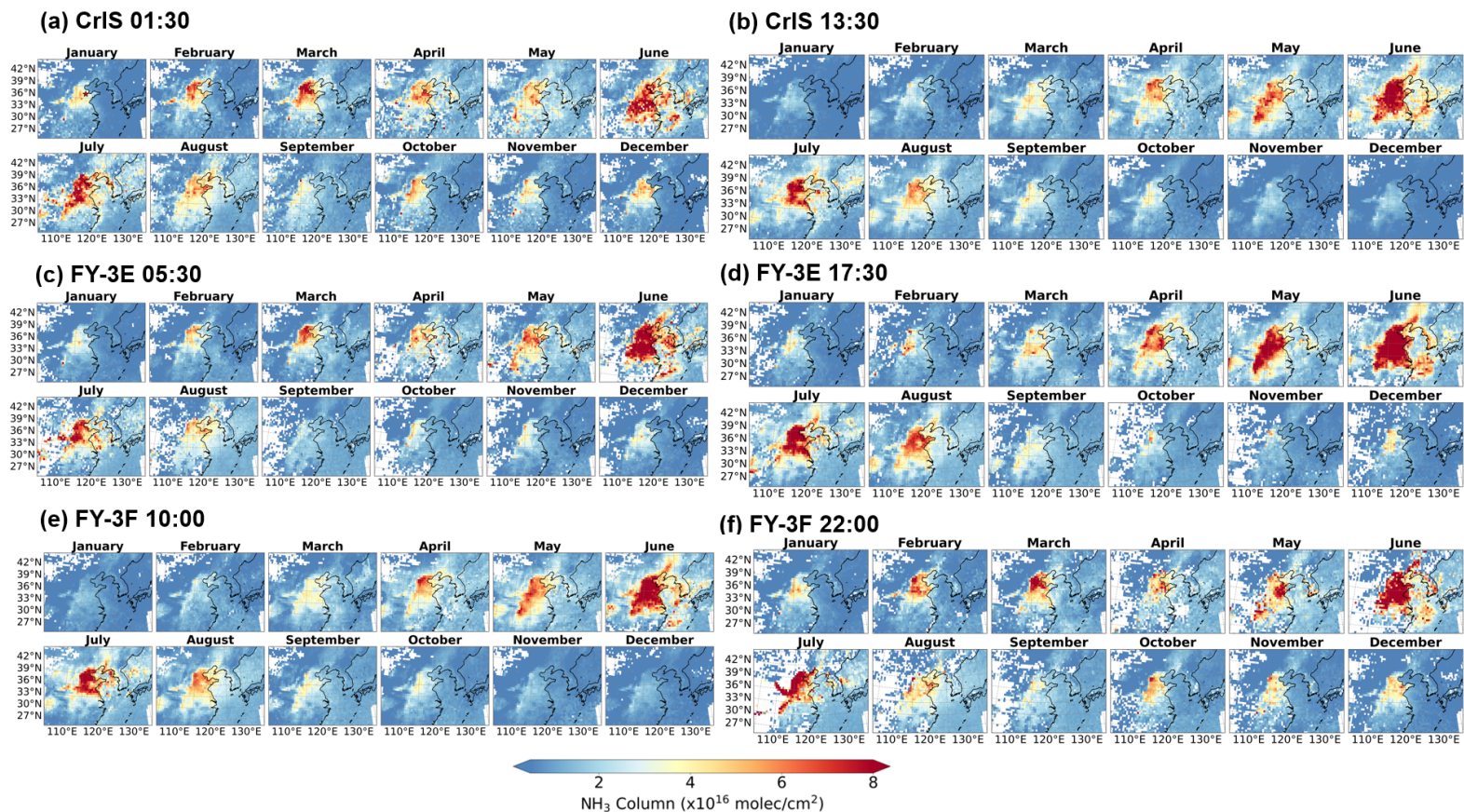
central U.S., Fig. 7 reveals the lowest overall  $\text{NH}_3$  columns among the three regions, with daytime spatial patterns spreading across the Corn Belt and Great Plains, and nighttime patterns contracting to smaller agricultural clusters.

300 The comparison between daytime and nighttime spatial patterns underscores the critical role of BLH in shaping  $\text{NH}_3$  distribution. Daytime maps display broader spatial coverage because higher BLH (typically 1–3 km during warm-season days) facilitates vertical and horizontal diffusion of  $\text{NH}_3$  away from emission sources. In contrast, nighttime maps show more localized  $\text{NH}_3$  columns, as lower BLH (often <500 m at night) traps emissions near the surface (Walker et al., 2006; Wang et al., 2019). This pattern is especially pronounced over the North China Plain, where Figs. 5b–5d show contiguous high- $\text{NH}_3$  zones across the plain, while Figs. 5a, 5e and 5f limit high columns to central agricultural districts. For the Indo-Gangetic Plain, 305 nighttime spatial maps also reveal persistent  $\text{NH}_3$  in the residual layer, an effect linked to BLH collapse in the evening, which traps  $\text{NH}_3$  at higher altitudes for several hours (Lonsdale et al., 2017; Kuang et al., 2020). This residual layer  $\text{NH}_3$  explains why some nighttime retrievals show broader coverage than expected, even with low BLH, and aligns with the observation by Clarisse et al. (2021) that  $\text{NH}_3$  vertical profile assumptions can impact nighttime retrieval accuracy.

To assess the impact of the filters on the retrieved  $\text{NH}_3$  diurnal variation, we perform an additional sensitivity analysis 310 using three filtering configurations: a loose filter with surface AVK > 0.1 and absolute TC > 3 K, the current hotspot filter with surface layer AVK value > 0.3 and absolute TC > 5 K, and a stricter filter with surface layer AVK value > 0.4 and absolute TC > 7 K. The remaining quality-control criteria are kept consistent among the three configurations. The resulting spatial distributions over the North China Plain and Indo-Gangetic Plain and the corresponding diurnal cycles are shown in the Supplementary. The total numbers of quality-controlled retrievals retained for each satellite under the different filtering 315 configurations are also reported in the subpanels. The three filtering configurations lead to different data-retention rates, as expected, but the major  $\text{NH}_3$  hotspot patterns remain spatially similar and the regional diurnal cycles are not substantially distorted. This indicates that the main diurnal features discussed here are not strongly affected by the selected absolute TC and surface AVK thresholds, although the absolute column values and sampling density remain sensitive to filtering strength.



320 Figure 4. Diurnal cycles of retrieved NH<sub>3</sub> columns from FY-3E, FY-3F and CrIS over (a) the North China Plain (118°E, 37°N), (b)  
 325 the Indo-Gangetic Plain (78°E, 28°N), and (c) the Central U.S. (100.5°W, 36.5°N). The locations of these three sites are indicated in  
 Figs. 5-7, respectively. Blue circles denote the mean values within the 2.5° × 2.5° grid, and the blue shaded area represents the  
 standard deviation for each overpass time. IASI retrieval results for the same region are overlaid for comparison: reddish purple  
 squares indicate IASI mean values, with error bars representing their standard deviation. The time axis is expressed in LST. The  
 diurnal variation of monthly mean planetary boundary layer height (BLH) is also plotted in purple.



330 **Figure 5.** Monthly mean  $\text{NH}_3$  columns ( $0.5^\circ \times 0.5^\circ$  grid) over the North China Plain retrieved by (a) CrIS at night overpasses (01:30 LST), (b) CrIS at daytime overpasses (13:30 LST), (c) FY-3E/HIRAS-II at dawn overpasses (05:30 LST), (d) FY-3E/HIRAS-II at dusk overpasses (17:30 LST), (e) FY-3F/HIRAS-II at morning overpasses (10:00 LST), and (f) FY-3F/HIRAS-II at night overpasses (22:00 LST), during 2024. The red star in the January panel of Fig. 5a indicates the location of the site (118°E, 37°N) analyzed in Figs. 4 and 9.

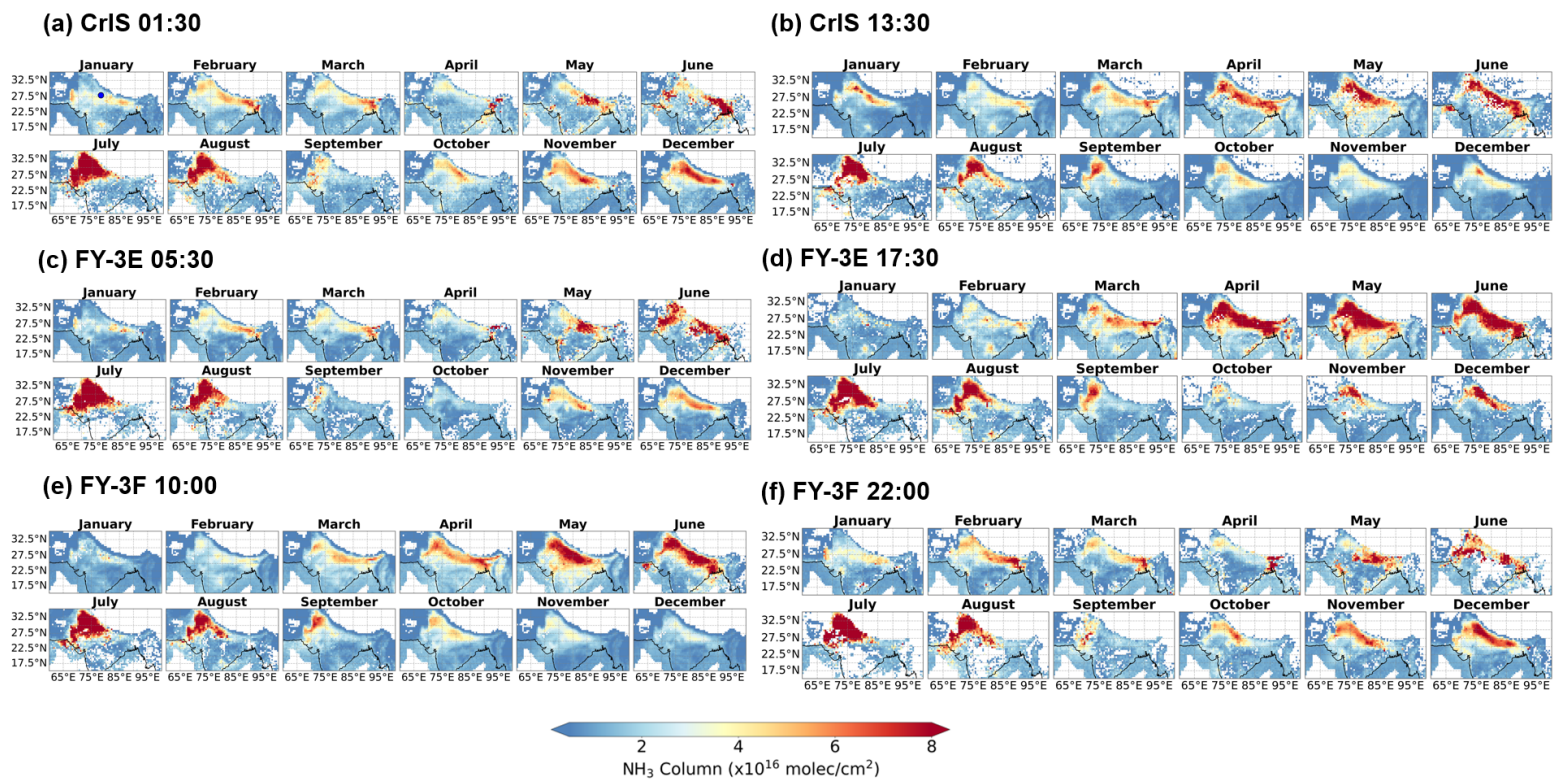
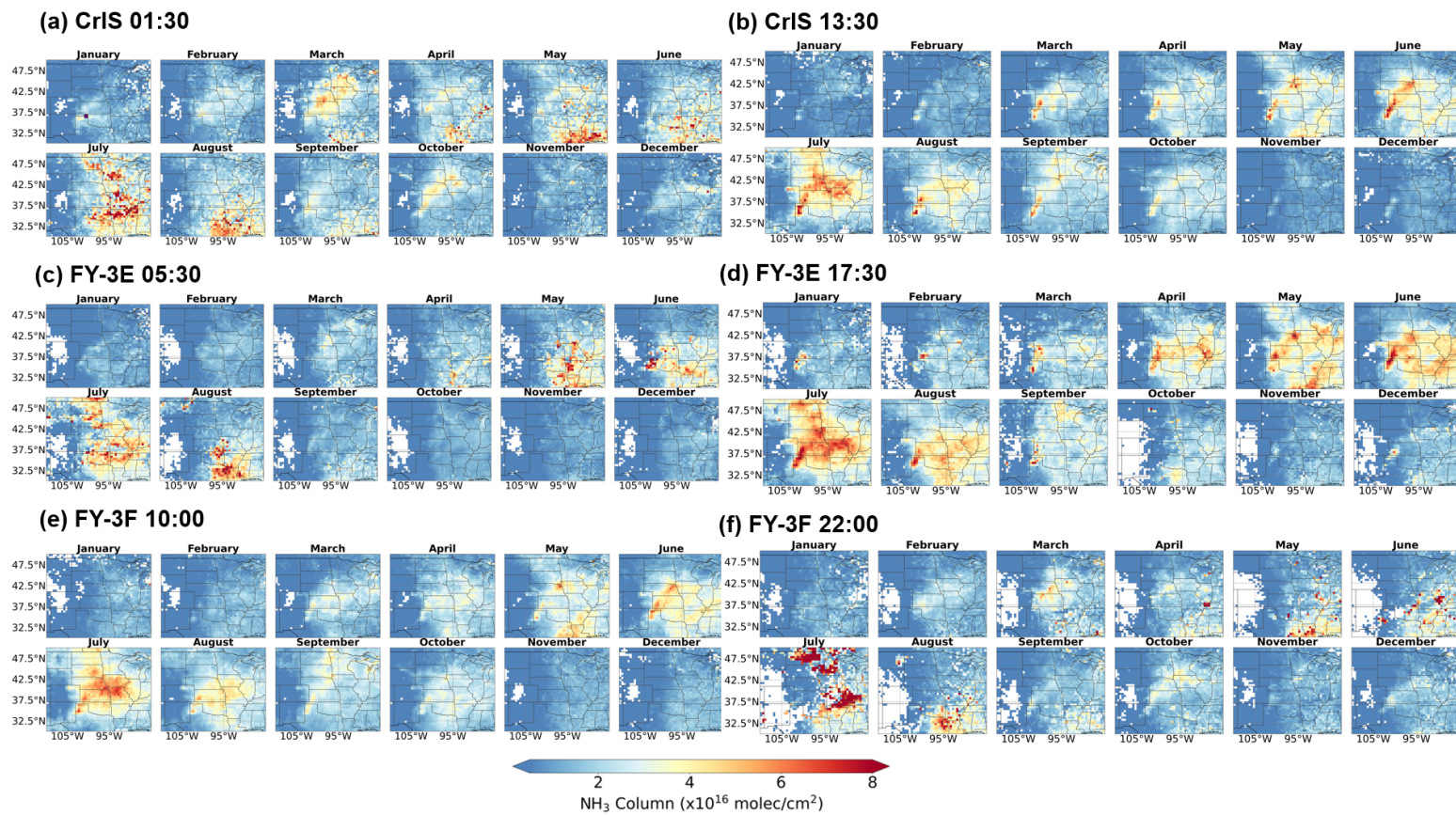


Figure 6. Same as Fig. 5, but for the Indo-Gangetic Plain. The blue circle in the January panel of Fig. 6a indicates the location of the site (78°E, 28°N) analyzed in Figs. 4 and 9.



335

Figure 7. Same as Fig. 5, but for the Central U.S. The purple square in the January panel of Fig. 7a indicates the location of the site (100.5°W, 36.5°N) analyzed in Figs. 4 and 9.

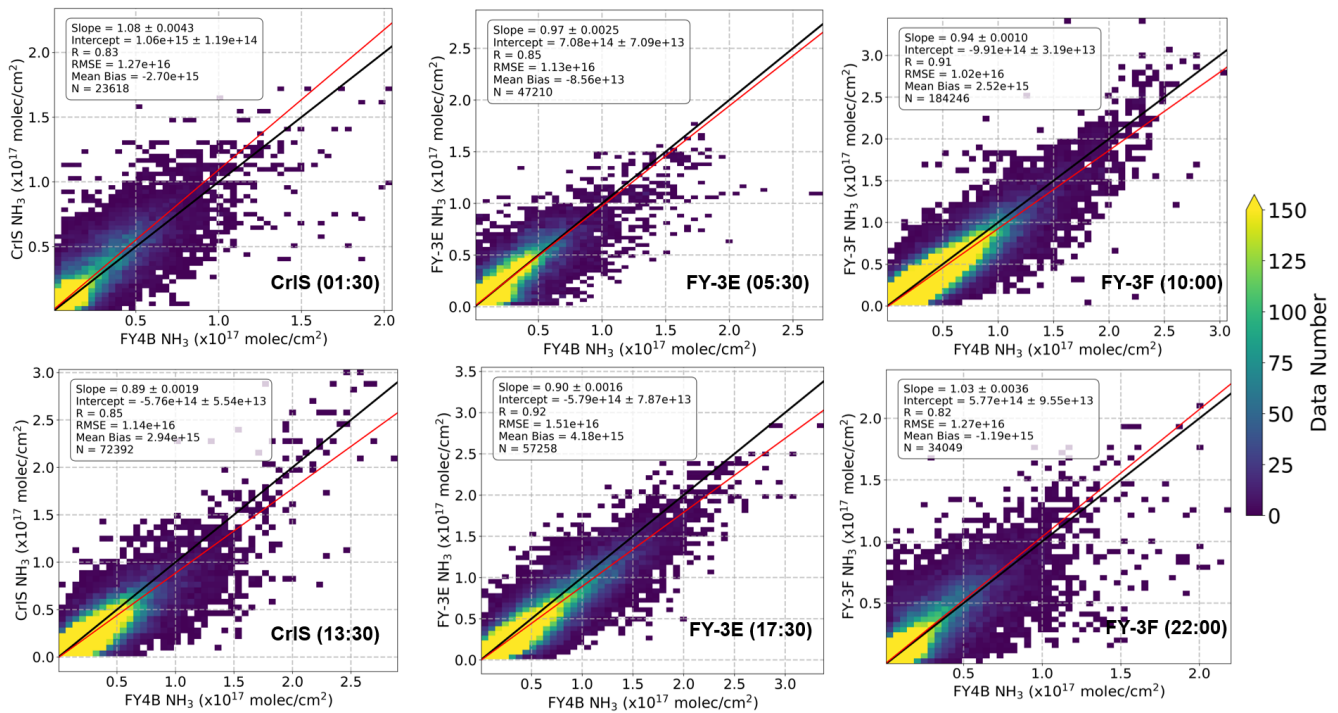
### 3.3 Cross-comparison with geostationary FY-4B/GIIRS and ground-based FTIR NH<sub>3</sub> observations

To evaluate the consistency of NH<sub>3</sub> column retrievals from the polar-orbiting constellation, we perform spatiotemporally  
340 collocated cross-comparisons between FY-3E/HIRAS-II, FY-3F/HIRAS-II, CrIS, and geostationary FY-4B/GIIRS retrievals.  
The comparisons are conducted over the Indo-Gangetic Plain (75°E–95°E, 15°N–35°N) and the North China Plain (110°E–  
130°E, 25°N–45°N), where strong NH<sub>3</sub> signals are frequently observed and FY-4B/GIIRS provides geostationary coverage.  
A polar-orbiting retrieval and a FY-4B/GIIRS retrieval are considered collocated when their longitude and latitude differences  
are both less than 0.5° and their observation time difference is less than 0.5 h. These thresholds are selected as a compromise  
345 between retaining sufficient matched samples and minimizing spatial and temporal representativeness differences.

The comparisons in Fig. 8 also show broad consistency across the matched local overpass periods sampled by the three  
polar-orbiting sensors. Here, the observational periods refer to the local-time periods of the polar-orbiting observations  
collocated with FY-4B/GIIRS, namely CrIS at 01:30/13:30, FY-3E/HIRAS-II at 05:30/17:30, and FY-3F/HIRAS-II at  
10:00/22:00. The agreement across these matched local-time periods indicates that the constellation retrievals are generally  
350 consistent with FY-4B/GIIRS over both nighttime/dawn and daytime/dusk observations, although the agreement is typically  
stronger during daytime because of larger thermal contrast and higher retrieval sensitivity.

We further perform seasonal comparisons between each polar-orbiting sensor and FY-4B/GIIRS using the same  
collocation and quality-filtering criteria. These results are shown in Fig. A2. The seasonal regression slopes mostly fall within  
the range of 0.7–1.1. The slopes slightly below unity in the annual comparison should not be interpreted as clear evidence of  
355 a persistent systematic bias in either FY-4B/GIIRS or the polar-orbiting retrievals. Instead, the remaining differences are likely  
due to their differences in retrieval sensitivity, collocation representativeness, sampling footprints, viewing geometry, and  
vertical sensitivity. These factors are particularly important for NH<sub>3</sub> because of its short atmospheric lifetime and strong spatial  
heterogeneity.

We also compare the polar-orbiting satellite retrievals with ground-based FTIR NH<sub>3</sub> column measurements at Hefei,  
360 China (Wang et al., 2022). Satellite retrievals within a 1° × 1° spatial window and a 1 h temporal window around the FTIR  
observations are averaged and compared with the corresponding measurements. The comparison is shown in Fig. A3. The  
satellite retrievals show reasonable consistency with the FTIR observations, although the number of collocated samples is  
limited, with slopes of  $0.87 \pm 0.22$ ,  $1.03 \pm 0.08$ , and  $1.13 \pm 0.18$  for FY-3E/HIRAS-II, FY-3F/HIRAS-II, and CrIS, respectively.  
The corresponding RMSE values range from  $7.80 \times 10^{15}$  to  $1.11 \times 10^{16}$  molec/cm<sup>2</sup>. Overall, the annual and seasonal FY-  
365 4B/GIIRS comparisons, together with the Hefei FTIR comparison, support the broad consistency of the LEO constellation  
retrievals in capturing major NH<sub>3</sub> spatial and temporal variability.



370 **Figure 8.** Comparisons of NH<sub>3</sub> columns between retrievals from polar-orbiting satellites (FY-3E/HIRAS-II, FY-3F/HIRAS-II and  
 375 CrIS) and geostationary satellite (FY-4B/GIIRS) over the Indo-Gangetic Plain (75°E-95°E, 15°N-35°N) and the North China Plain (110°E-130°E, 25°N-45°N) at different times of the day in 2024. Observations are collocated when the differences in longitude and latitude are both less than 0.5° and the observation-time difference is less than 0.5 hours. The black dashed line represents the 1:1 equivalence line, with the red line indicating the orthogonal distance regression (ODR) fit. The fit's slope, intercept, correlation coefficient (R), root mean square error (RMSE), mean bias (calculated as polar satellite retrievals minus geostationary satellite retrievals), and the number of collocated samples are also provided.

### 3.4 Diurnal variations of the surface AVK, the retrieval uncertainty and the TC

Fig. 9 presents the diurnal and seasonal dynamics of surface AVK, TC, and column retrieval uncertainty over three representative hotspots, located in the North China Plain (118°E, 37°N), the Indo-Gangetic Plain (78°E, 28°N), and the Central U.S. (100.5°W, 36.5°N). The statistics are derived from FY-3E/HIRAS-II, FY-3F/HIRAS-II, and CrIS retrievals within 2.5°  
 380 × 2.5° boxes and are shown as monthly averages for January, April, July, and October across six local overpass times. To clarify the robustness of these monthly averages, the number of valid retrievals used for each region, month, and overpass time is provided in Table S2. Monthly means are shown only when more than 10 quality-controlled retrievals are available.

TC exhibits a clear diurnal pattern across all regions. It generally reaches positive maxima during midday overpasses at 10:00–13:30 LST, with peak values of about 10–14 K over the North China Plain and about 17–20 K over the Indo-Gangetic  
 385 Plain and the Central U.S. in warm months. Nighttime and early-morning TC values are often negative, especially over the

Indo-Gangetic Plain and the Central U.S. in January, April, and October, while the North China Plain shows weaker negative TC in January and positive TC throughout July and October. These seasonal contrasts indicate that warm-season daytime observations generally provide strong positive TC, whereas nighttime observations often occur under negative TC conditions

390 The surface layer value of column AVK, which quantifies the observational information content related to near-surface NH<sub>3</sub>, also shows pronounced diurnal and seasonal variability. Midday overpasses generally provide useful sensitivity to near-surface NH<sub>3</sub> variations, with surface-layer column AVK values mostly ranging from about 0.5 to 0.9 at 10:00–13:30, although the peak surface layer column AVK does not always occur at midday. The Indo-Gangetic Plain exhibits pronounced diurnal swings, with July midday surface layer column AVK reaching 0.6, while the Central U.S. shows moderate values of 0.57–0.70 at 10:00–13:30 but higher values during some nighttime overpasses. Overall, warm-season daytime conditions  
395 generally provide favorable observational constraints for NH<sub>3</sub> retrievals, although the surface layer value of column AVK can be high under negative TC conditions.

Column retrieval uncertainty generally decreases under conditions with larger absolute TC and higher surface AVK, but this relationship is not purely inverse and should not be interpreted as strictly monotonic. In particular, strongly negative TC can also enhance thermal infrared sensitivity because absorption-like spectral features may become emission-like features,  
400 as shown for lower-tropospheric pollution retrievals by Boynard et al. (2014). Therefore, TC should be interpreted together with AVK and retrieval uncertainty, rather than as a standalone monotonic sensitivity indicator.

Daytime bins often contain more valid retrievals than nighttime or dusk/evening bins, but the pattern is not uniform across regions and months (Table S2). Some bins have relatively sparse sampling, such as the Indo-Gangetic Plain in July at 05:30 and 22:00 and the Central U.S. in October at 17:30, whereas other daytime bins contain more than 1000 valid retrievals.  
405 These differences mainly reflect the combined effects of cloud screening and sensitivity-related quality filters.

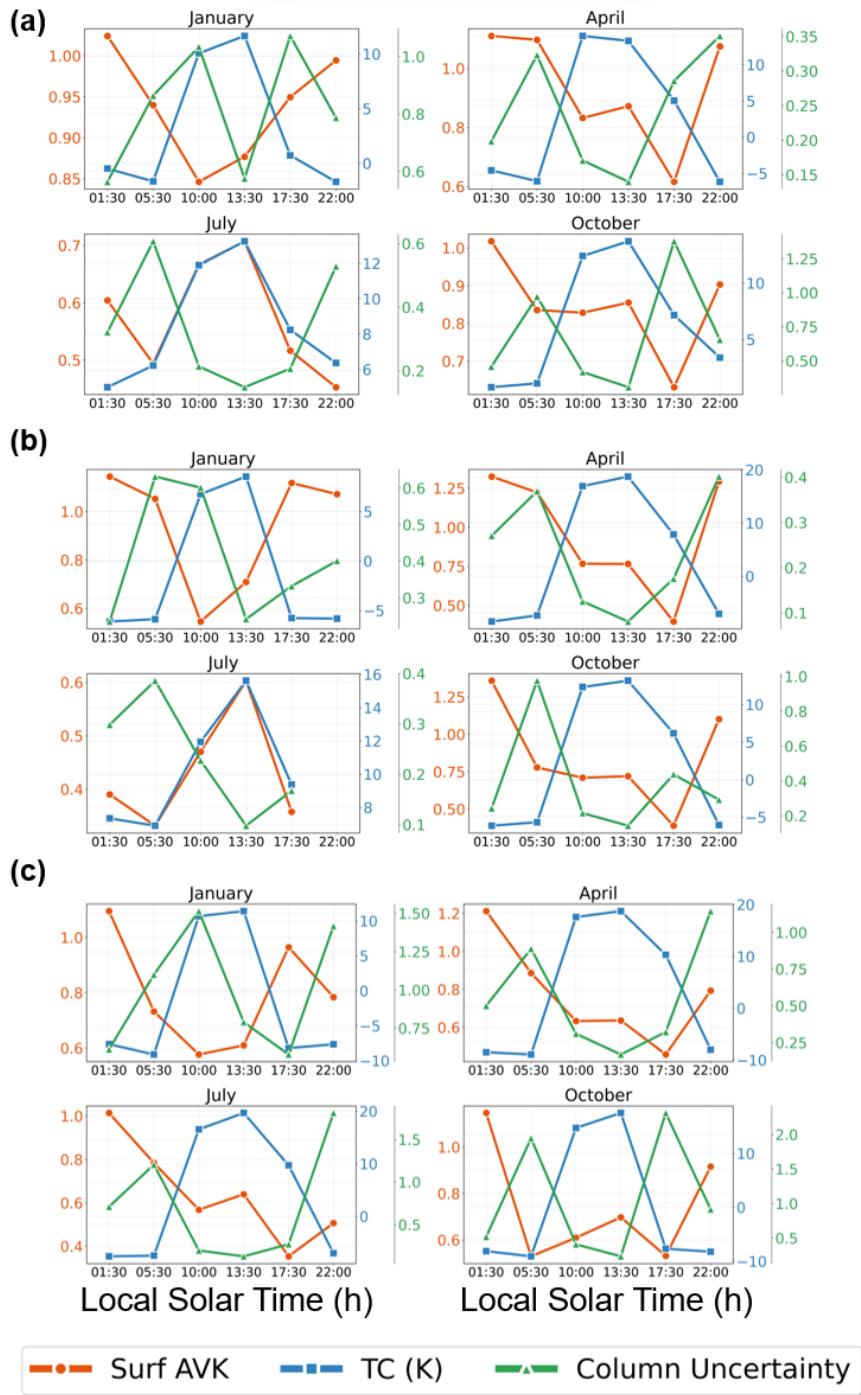


Figure 9. Diurnal cycles of surface AVK, TC and column retrieval uncertainty from FY-3E, FY-3F and CrIS over three hotspots in (a) the North China Plain (118°E, 37°N), (b) the Indo-Gangetic Plain (78°E, 28°N), and (c) the Central U.S. (100.5°W, 36.5°N). The number of valid retrievals used for each monthly mean is provided in Table S2.

410

## 4 Conclusions

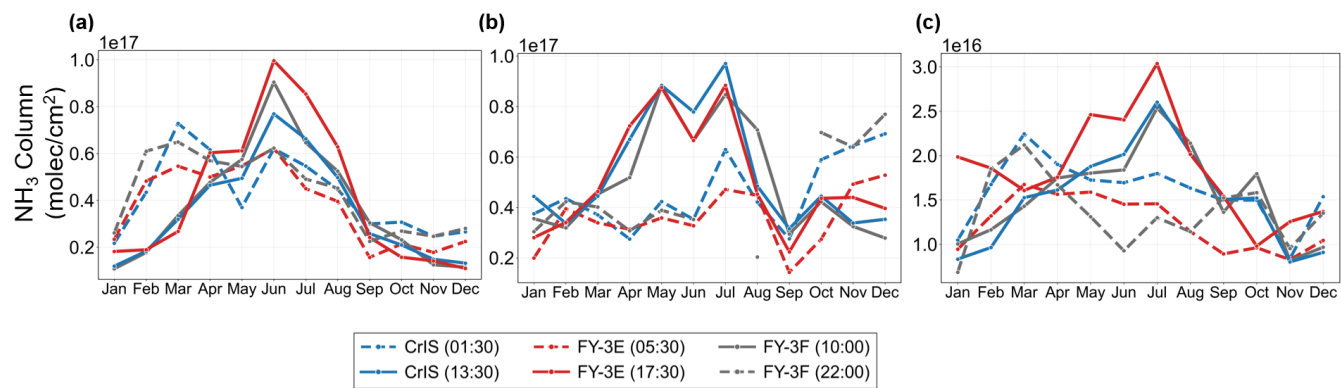
This study develops a global monitoring framework by integrating three polar-orbiting hyperspectral infrared sounders, including FY-3E/HIRAS-II in a dawn-dusk orbit, FY-3F/HIRAS-II in a mid-morning orbit, and CrIS in an afternoon orbit. This constellation achieves quasi-geostationary-like coverage, enabling six global NH<sub>3</sub> column retrievals per day at approximately 4-hour intervals based on the optimal estimation method. This framework successfully captures the spatial, diurnal, and seasonal dynamics of tropospheric NH<sub>3</sub> worldwide, with elevated columns consistently identified over major source regions. Annual and seasonal cross-comparisons with geostationary FY-4B/GIIRS show broad consistency between the LEO constellation retrievals and GIIRS over the matched local overpass periods, including CrIS at 01:30/13:30, FY-3E/HIRAS-II at 05:30/17:30, and FY-3F/HIRAS-II at 10:00/22:00. An additional comparison with ground-based FTIR observations at Hefei provides independent support for the reliability and consistency of the retrievals.

The key findings indicate that temperature-dependent volatilization, boundary-layer dynamics, and agricultural activity patterns jointly regulate the diurnal and seasonal variability of NH<sub>3</sub>. Differences among regions are further modulated by source strength, fertilizer and livestock management practices, meteorological conditions, and atmospheric chemical processing. The constellation effectively addresses the longstanding gap in high-frequency NH<sub>3</sub> observations over regions lacking geostationary satellite coverage, providing a comprehensive dataset for global NH<sub>3</sub> cycling research.

Looking forward, the upcoming integration of FY-3H/HIRAS-II, launched at the end of 2025, equipped with the same HIRAS-II sensor as FY-3E and FY-3F, is expected to improve the homogeneity of the FY-based constellation and further enhance data consistency and spatiotemporal coverage. This refined system holds strong potential to advance NH<sub>3</sub> emission quantification, improve parameterizations in global climate and air quality models, and support evidence-based management of anthropogenic sources. Future work could focus on optimizing NH<sub>3</sub> vertical profile parametrization, cross-calibrating between sensors onboard different satellites for enhanced retrieval accuracy and consistency, and expanding the constellation's applications to investigate the links between NH<sub>3</sub>, aerosol formation, acid deposition, and ecosystem impacts. To summarize, this framework demonstrates the value of the synergistic use of polar-orbiting satellites for strengthening global atmospheric composition monitoring and providing observational support for mitigating NH<sub>3</sub>-related environmental and climate effects.

435

## Appendix A



440 **Figure A1. Seasonal time series of retrieved  $\text{NH}_3$  columns over (a) the North China Plain, (b) the Indo-Gangetic Plain and (c) the Central U.S.**

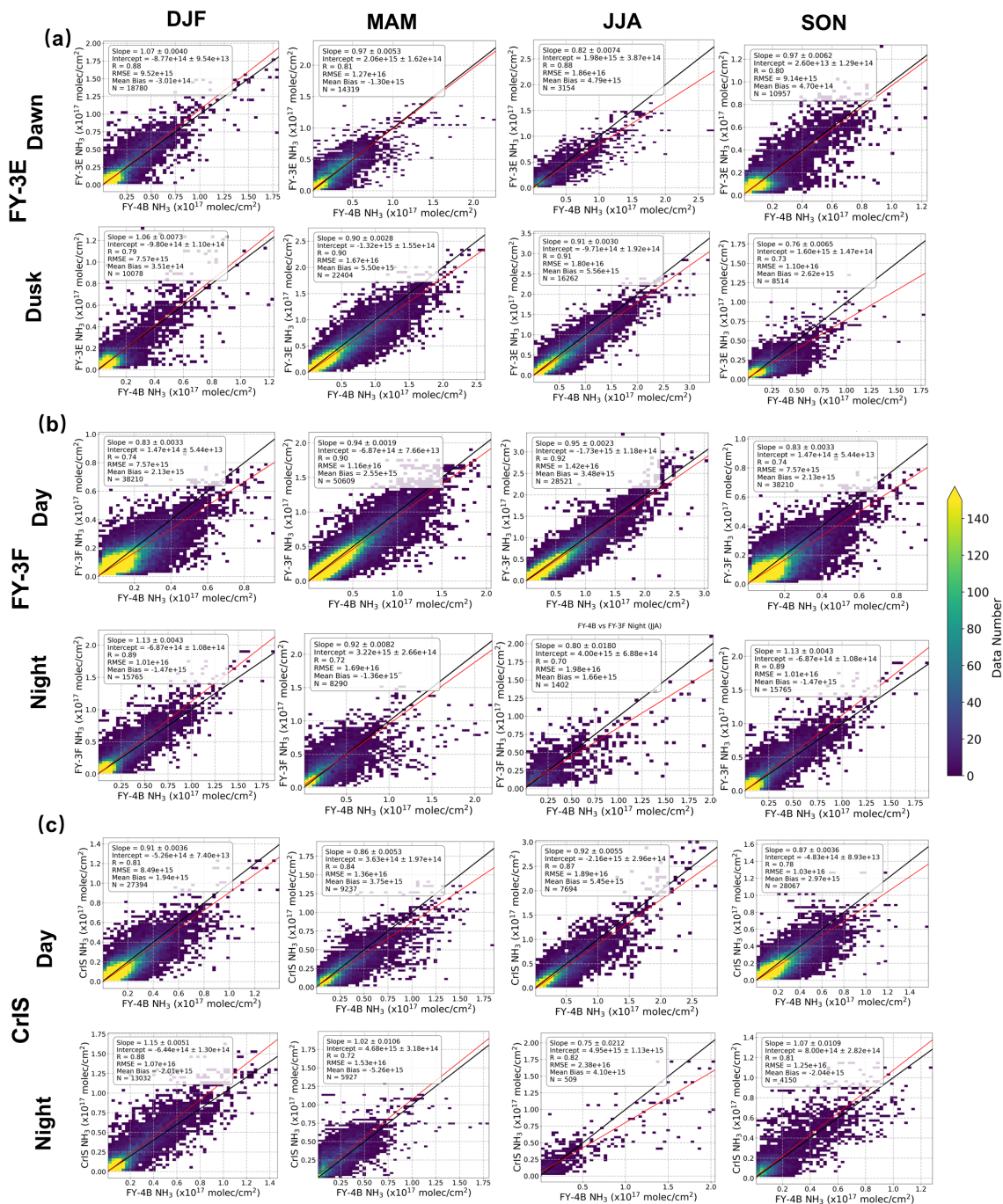
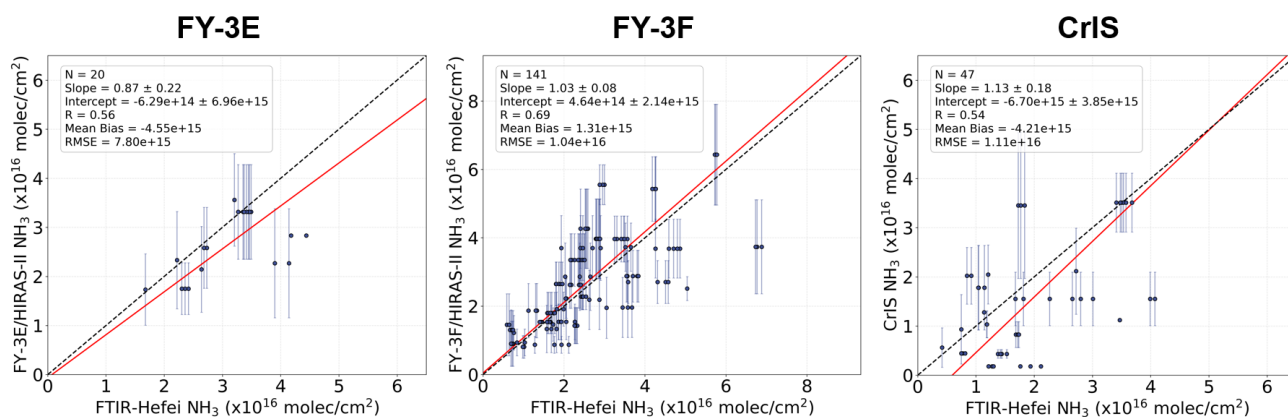


Figure A2. Same as Fig. 8, but for seasonal comparisons between FY-3E/HIRAS-II (a), FY-3F/HIRAS-II (b), CrIS (c) and FY-4B/GIIRS over the Indo-Gangetic Plain and the North China Plain. DJF, MAM, JJA, and SON denote December–January–February, March–April–May, June–July–August, and September–October–November, respectively. The black solid line represents the 1:1 line, and the red solid line indicates the orthogonal distance regression (ODR) fit. The slope, intercept, correlation coefficient (R), root mean square error (RMSE), mean bias, and number of collocated samples are provided in each panel.



450 **Figure A3. Validations with ground-based FTIR in Hefei, China.** The black dashed line represents the 1:1 equivalence line, with the red line indicating the orthogonal distance regression (ODR) fit. The fit's slope, intercept, correlation coefficient (R), root mean square error (RMSE), mean bias (calculated as polar satellite retrievals minus ground-based measurements), and number of collocated samples are also provided. The dot represents the mean value of satellite-retrieved NH<sub>3</sub> columns and the error bar represents 1 standard deviation. If there is only one match point, the error bars are not displayed.

#### 455 **Data availability**

The FY-3E and FY-3F NH<sub>3</sub> retrieval datasets are publicly available at ZENODO (<https://doi.org/10.5281/zenodo.18359451> and <https://doi.org/10.5281/zenodo.18366114>, respectively). Currently, the FY-3E dataset is available from January 2023 to December 2024, and the FY-3F dataset is available from January to December 2024. The GIIRS NH<sub>3</sub> data (from July 2022 to June 2025) used in this study are publicly available on Zenodo (<https://doi.org/10.5281/zenodo.17193848>). Further updates on  
 460 FengYun NH<sub>3</sub> data will be provided on the project website (<https://fengyunair.github.io/>). FengYun satellite Level 1 data are publicly available from the FengYun Satellite Data Center at <http://satellite.nsmc.org.cn/portalsite/default.aspx>. The IASI NH<sub>3</sub> ANNI V4.0 product is available from the AERIS data infrastructure (<https://iasi.aeris-data.fr/>). The CrIS L1 spectra are publicly available from <https://search.earthdata.nasa.gov/>.

#### **Author contributions**

465 ZZ designed the experiments, and JH carried them out. ZZ and JH developed the model code and JH performed the simulations. MS and RZ assisted the satellite data pre-processing and results analysis. JH prepared the manuscript with contributions from all co-authors.

## **Competing interests**

At least one of the (co-)authors is a member of the editorial board of Atmospheric Measurement Techniques.

## 470 **Acknowledgements**

We gratefully acknowledge Drs. Chengli Qi, Lu Lee, Xiuqing Hu, and Feng Lu from the National Meteorological Satellite Center of China for their guidance on using the FengYun hyperspectral infrared spectra observations. We would also like to thank Drs. Cathy Clerbaux, Lieven Clarisse and Martin Van Damme for making the IASI NH<sub>3</sub> data publicly available. We thank Dr. Wei Wang from the Chinese Academy of Sciences for providing the Hefei-FTIR NH<sub>3</sub> data and Dr. Mark Shephard  
475 from Environment and Climate Change Canada for discussion on interpreting the column averaging kernel of NH<sub>3</sub> column retrievals.

## **Financial support**

Z.-C. Zeng acknowledges funding from the National Natural Science Foundation of China (grant nos. 42275142), the National Key R&D Program of China (grant no. 2026YFE0102400). This work was also supported by High-performance Computing  
480 Platform of Peking University.

## References

- Abbatt, J. P. D., Benz, S., Cziczo, D. J., Kanji, Z., Lohmann, U., and Möhler, O.: Solid Ammonium Sulfate Aerosols as Ice Nuclei: A Pathway for Cirrus Cloud Formation, *Science*, 313, 1770–1773, <https://doi.org/10.1126/science.1129726>, 2006.
- 485 Adams, P. J., Seinfeld, J. H., Koch, D., Mickley, L., and Jacob, D.: General circulation model assessment of direct radiative forcing by the sulfate-nitrate-ammonium-water inorganic aerosol system, *J Geophys Res-Atmos*, 106, 1097–1111, <https://doi.org/10.1029/2000JD900512>, 2001.
- Bauduin, S., Clarisse, L., Theunissen, M., George, M., Hurtmans, D., Clerbaux, C., and Coheur, P.-F.: IASI's sensitivity to near-surface carbon monoxide (CO): Theoretical analyses and retrievals on test cases, *J. Quant. Spectrosc. Radiat. Transf.*, 490 189, 428–440, <https://doi.org/10.1016/j.jqsrt.2016.12.022>, 2017.
- Beer, R., Shephard, M. W., Kulawik, S. S., Clough, S. A., Eldering, A., Bowman, K. W., Sander, S. P., Fisher, B. M., Payne, V. H., Luo, M., Osterman, G. B., and Worden, J. R.: First satellite observations of lower tropospheric ammonia and methanol, *Geophys. Res. Lett.*, 35, 2008GL033642, <https://doi.org/10.1029/2008GL033642>, 2008.
- 495 Behera, S. N., Sharma, M., Aneja, V. P., and Balasubramanian, R.: Ammonia in the atmosphere: a review on emission sources, atmospheric chemistry and deposition on terrestrial bodies, *Environ. Sci. Pollut. Res.*, 20, 8092–8131, <https://doi.org/10.1007/s11356-013-2051-9>, 2013.
- Boynard, A., Clerbaux, C., Clarisse, L., Safieddine, S., Pommier, M., Van Damme, M., Bauduin, S., Oudot, C., Hadji-Lazaro, J., Hurtmans, D., and Coheur, P.: First simultaneous space measurements of atmospheric pollutants in the boundary layer from IASI: A case study in the North China Plain, *Geophys. Res. Lett.*, 41, 645–651, <https://doi.org/10.1002/2013GL058333>, 2014.
- 500 Clarisse, L., Clerbaux, C., Dentener, F., Hurtmans, D., and Coheur, P.-F.: Global ammonia distribution derived from infrared satellite observations, *Nat. Geosci.*, 2, 479–483, <https://doi.org/10.1038/ngeo551>, 2009.
- Clarisse, L., Shephard, M. W., Dentener, F., Hurtmans, D., Cady-Pereira, K., Karagulian, F., Van Damme, M., Clerbaux, C., and Coheur, P.: Satellite monitoring of ammonia: A case study of the San Joaquin Valley, *J. Geophys. Res.-Atmos.*, 115, 2009JD013291, <https://doi.org/10.1029/2009JD013291>, 2010.
- 505 Clarisse, L., Clerbaux, C., Franco, B., Hadji-Lazaro, J., Whitburn, S., Kopp, A. K., Hurtmans, D., and Coheur, P. -F.: A Decadal Data Set of Global Atmospheric Dust Retrieved From IASI Satellite Measurements, *J. Geophys. Res.-Atmos.*, 124, 1618–1647, <https://doi.org/10.1029/2018JD029701>, 2019.
- Clarisse, L., Van Damme, M., Hurtmans, D., Franco, B., Clerbaux, C., and Coheur, P.: The Diel Cycle of NH<sub>3</sub> Observed From the FY-4A Geostationary Interferometric Infrared Sounder (GIIRS), *Geophys. Res. Lett.*, 48, e2021GL093010, 510 <https://doi.org/10.1029/2021GL093010>, 2021.
- Dammers, E., Schaap, M., Haaima, M., Palm, M., Wichink Kruit, R. J., Volten, H., Hensen, A., Swart, D., and Erisman, J. W.: Measuring atmospheric ammonia with remote sensing campaign: Part 1 – Characterisation of vertical ammonia concentration profile in the centre of The Netherlands, *Atmos. Environ.*, 169, 97–112, <https://doi.org/10.1016/j.atmosenv.2017.08.067>, 2017.
- 515 De Mazière, M., Thompson, A. M., Kurylo, M. J., Wild, J. D., Bernhard, G., Blumenstock, T., Braathen, G. O., Hannigan, J. W., Lambert, J.-C., Leblanc, T., McGee, T. J., Nedoluha, G., Petropavlovskikh, I., Seckmeyer, G., Simon, P. C., Steinbrecht, W., and Strahan, S. E.: The Network for the Detection of Atmospheric Composition Change (NDACC): history, status and perspectives, *Atmos. Chem. Phys.*, 18, 4935–4964, <https://doi.org/10.5194/acp-18-4935-2018>, 2018.

- 520 Ding, J., Van Der A, R., Eskes, H., Dammers, E., Shephard, M., Wichink Kruit, R., Guevara, M., and Tarrason, L.: Ammonia emission estimates using CrIS satellite observations over Europe, *Atmos. Chem. Phys.*, 24, 10583–10599, <https://doi.org/10.5194/acp-24-10583-2024>, 2024.
- Erisman, J. W., Sutton, M. A., Galloway, J., Klimont, Z., and Winiwarer, W.: How a century of ammonia synthesis changed the world, *Nat. Geosci.*, 1, 636–639, <https://doi.org/10.1038/ngeo325>, 2008.
- 525 Erisman, J. W., Galloway, J. N., Seitzinger, S., Bleeker, A., Dise, N. B., Petrescu, A. M. R., Leach, A. M., and De Vries, W.: Consequences of human modification of the global nitrogen cycle, *Philos. Trans. R. Soc. B Biol. Sci.*, 368, 20130116, <https://doi.org/10.1098/rstb.2013.0116>, 2013.
- Ernst, J. W. and Massey, H. F.: The Effects of Several Factors on Volatilization of Ammonia Formed from Urea in the Soil, *Soil Sci. Soc. Am. J.*, 24, 87–90, <https://doi.org/10.2136/sssaj1960.03615995002400020007x>, 1960.
- 530 Fowler, D., Coyle, M., Skiba, U., Sutton, M. A., Cape, J. N., Reis, S., Sheppard, L. J., Jenkins, A., Grizzetti, B., Galloway, J. N., Vitousek, P., Leach, A., Bouwman, A. F., Butterbach-Bahl, K., Dentener, F., Stevenson, D., Amann, M., and Voss, M.: The global nitrogen cycle in the twenty-first century, *Philos. Trans. R. Soc. B Biol. Sci.*, 368, 20130164, <https://doi.org/10.1098/rstb.2013.0164>, 2013.
- Galloway, J. N., Aber, J. D., Erisman, J. W., Seitzinger, S. P., Howarth, R. W., Cowling, E. B., and Cosby, B. J.: The Nitrogen Cascade, *BioScience*, 53, 341, [https://doi.org/10.1641/0006-3568\(2003\)053%5B0341:TNC%5D2.0.CO;2](https://doi.org/10.1641/0006-3568(2003)053%5B0341:TNC%5D2.0.CO;2), 2003.
- 535 Galloway, J. N., Dentener, F. J., Capone, D. G., Boyer, E. W., Howarth, R. W., Seitzinger, S. P., Asner, G. P., Cleveland, C. C., Green, P. A., Holland, E. A., Karl, D. M., Michaels, A. F., Porter, J. H., Townsend, A. R., and Vorosmarty, C. J.: Nitrogen Cycles: Past, Present, and Future, *Biogeochemistry*, 70, 153–226, <https://doi.org/10.1007/s10533-004-0370-0>, 2004.
- 540 Guendouz, N., Viatte, C., Zeng, Z., Boynard, A., Safieddine, S., Standfuss, C., Turquety, S., Van Damme, M., Clarisse, L., Coheur, P., Sheng, M., Armante, R., Prunet, P., and Clerbaux, C.: Monitoring Atmospheric Ammonia From Geostationary Orbit: Contributions of GIIRS-B and IRS Remote Sensors, *J. Geophys. Res.-Atmos.*, 131, e2025JD046139, <https://doi.org/10.1029/2025JD046139>, 2026.
- Guo, H., Otjes, R., Schlag, P., Kiendler-Scharr, A., Nenes, A., and Weber, R. J.: Effectiveness of ammonia reduction on control of fine particle nitrate, *Atmos. Chem. Phys.*, 18, 12241–12256, <https://doi.org/10.5194/acp-18-12241-2018>, 2018.
- 545 Hempel, S., Saha, C. K., Fiedler, M., Berg, W., Hansen, C., Amon, B., and Amon, T.: Non-linear temperature dependency of ammonia and methane emissions from a naturally ventilated dairy barn, *Biosyst. Eng.*, 145, 10–21, <https://doi.org/10.1016/j.biosystemseng.2016.02.006>, 2016.
- Holmlund, K., Grandell, J., Schmetz, J., Stuhlmann, R., Bojkov, B., Munro, R., Lekouara, M., Coppens, D., Viticchie, B., August, T., Theodore, B., Watts, P., Dobber, M., Fowler, G., Bojinski, S., Schmid, A., Salonen, K., Tjemkes, S., Aminou, D., and Blythe, P.: Meteosat Third Generation (MTG): Continuation and Innovation of Observations from Geostationary Orbit, *Bull. Am. Meteorol. Soc.*, 102, E990–E1015, <https://doi.org/10.1175/BAMS-D-19-0304.1>, 2021.
- 550 Hua, J., Liu, S., Qi, C., Wu, S., Lee, L., Hu, X., Zhao, X., Strong, K., Flood, V., Franco, B., Clarisse, L., Clerbaux, C., Wunch, D., Roehl, C., Wennberg, P., and Zeng, Z.-C.: Observing carbon monoxide and volatile organic compounds from Canadian wildfires in 2023 from FengYun-3E/HIRAS-II in a dawn-dusk sun-synchronous orbit, *Remote Sens. Environ.*, 327, 114829, <https://doi.org/10.1016/j.rse.2025.114829>, 2025.
- 555 Isaksen, I. S. A., Granier, C., Myhre, G., Berntsen, T. K., Dalsøren, S. B., Gauss, M., Klimont, Z., Benestad, R., Bousquet, P., Collins, W., Cox, T., Eyring, V., Fowler, D., Fuzzi, S., Jöckel, P., Laj, P., Lohmann, U., Maione, M., Monks, P., Prevot, A. S.

- H., Raes, F., Richter, A., Rognerud, B., Schulz, M., Shindell, D., Stevenson, D. S., Storelvmo, T., Wang, W.-C., Van Weele, M., Wild, M., and Wuebbles, D.: Atmospheric composition change: Climate–Chemistry interactions, *Atmos. Environ.*, 43, 5138–5192, <https://doi.org/10.1016/j.atmosenv.2009.08.003>, 2009.
- 560 Jiménez, E., Cabañas, B., and Lefebvre, G. (Eds.): *Environment, Energy and Climate Change I: Environmental Chemistry of Pollutants and Wastes*, Springer International Publishing, Cham, <https://doi.org/10.1007/978-3-319-12907-5>, 2015.
- Kuang, Y., Xu, W., Lin, W., Meng, Z., Zhao, H., Ren, S., Zhang, G., Liang, L., and Xu, X.: Explosive morning growth phenomena of NH<sub>3</sub> on the North China Plain: Causes and potential impacts on aerosol formation, *Environ. Pollut.*, 257, 113621, <https://doi.org/10.1016/j.envpol.2019.113621>, 2020.
- 565 Li, Z., Sun, K., Guan, K., Wang, S., Peng, B., Clarisse, L., Van Damme, M., Coheur, P.-F., Cady-Pereira, K., Shephard, M. W., Zondlo, M., and Moore, D.: Ammonia emissions and depositions over the contiguous United States derived from IASI and CrIS using the directional derivative approach, *Atmos. Chem. Phys.*, 26, 703–721, <https://doi.org/10.5194/acp-26-703-2026>, 2026.
- 570 Lindaas, J., Pollack, I. B., Calahorrano, J. J., O’Dell, K., Garofalo, L. A., Pothier, M. A., Farmer, D. K., Kreidenweis, S. M., Campos, T., Flocke, F., Weinheimer, A. J., Montzka, D. D., Tyndall, G. S., Apel, E. C., Hills, A. J., Hornbrook, R. S., Palm, B. B., Peng, Q., Thornton, J. A., Permar, W., Wielgasz, C., Hu, L., Pierce, J. R., Collett, J. L., Sullivan, A. P., and Fischer, E. V.: Empirical Insights Into the Fate of Ammonia in Western U.S. Wildfire Smoke Plumes, *J. Geophys. Res.-Atmos.*, 126, e2020JD033730, <https://doi.org/10.1029/2020JD033730>, 2021.
- 575 Liu, M., Huang, X., Song, Y., Xu, T., Wang, S., Wu, Z., Hu, M., Zhang, L., Zhang, Q., Pan, Y., Liu, X., and Zhu, T.: Rapid SO<sub>2</sub> emission reductions significantly increase tropospheric ammonia concentrations over the North China Plain, *Atmos. Chem. Phys.*, 18, 17933–17943, <https://doi.org/10.5194/acp-18-17933-2018>, 2018.
- Liu, X., Zhang, Y., Han, W., Tang, A., Shen, J., Cui, Z., Vitousek, P., Erisman, J. W., Goulding, K., Christie, P., Fangmeier, A., and Zhang, F.: Enhanced nitrogen deposition over China, *Nature*, 494, 459–462, <https://doi.org/10.1038/nature11917>, 2013.
- 580 Lonsdale, C. R., Hegarty, J. D., Cady-Pereira, K. E., Alvarado, M. J., Henze, D. K., Turner, M. D., Capps, S. L., Nowak, J. B., Neuman, J. A., Middlebrook, A. M., Bahreini, R., Murphy, J. G., Markovic, M. Z., VandenBoer, T. C., Russell, L. M., and Scarino, A. J.: Modeling the diurnal variability of agricultural ammonia in Bakersfield, California, during the CalNex campaign, *Atmos. Chem. Phys.*, 17, 2721–2739, <https://doi.org/10.5194/acp-17-2721-2017>, 2017.
- 585 Luo, Z., Zhang, Y., Chen, W., Van Damme, M., Coheur, P.-F., and Clarisse, L.: Estimating global ammonia (NH<sub>3</sub>) emissions based on IASI observations from 2008 to 2018, *Atmos. Chem. Phys.*, 22, 10375–10388, <https://doi.org/10.5194/acp-22-10375-2022>, 2022.
- Lutsch, E., Strong, K., Jones, D. B. A., Ortega, I., Hannigan, J. W., Dammers, E., Shephard, M. W., Morris, E., Murphy, K., Evans, M. J., Parrington, M., Whitburn, S., Van Damme, M., Clarisse, L., Coheur, P., Clerbaux, C., Croft, B., Martin, R. V., Pierce, J. R., and Fisher, J. A.: Unprecedented Atmospheric Ammonia Concentrations Detected in the High Arctic From the 2017 Canadian Wildfires, *J. Geophys. Res.-Atmos.*, 124, 8178–8202, <https://doi.org/10.1029/2019JD030419>, 2019.
- 590 Myhre, G., Samset, B. H., Schulz, M., Balkanski, Y., Bauer, S., Berntsen, T. K., Bian, H., Bellouin, N., Chin, M., Diehl, T., Easter, R. C., Feichter, J., Ghan, S. J., Hauglustaine, D., Iversen, T., Kinne, S., Kirkevåg, A., Lamarque, J.-F., Lin, G., Liu, X., Lund, M. T., Luo, G., Ma, X., Van Noije, T., Penner, J. E., Rasch, P. J., Ruiz, A., Seland, Ø., Skeie, R. B., Stier, P., Takemura, T., Tsigaridis, K., Wang, P., Wang, Z., Xu, L., Yu, H., Yu, F., Yoon, J.-H., Zhang, K., Zhang, H., and Zhou, C.: Radiative forcing of the direct aerosol effect from AeroCom Phase II simulations, *Atmos. Chem. Phys.*, 13, 1853–1877, <https://doi.org/10.5194/acp-13-1853-2013>, 2013.

- Perrone, D.: Groundwater Overreliance Leaves Farmers and Households High and Dry, *One Earth*, 2, 214–217, <https://doi.org/10.1016/j.oneear.2020.03.001>, 2020.
- 600 Saraswati, Sharma, S. K., and Mandal, T. K.: Five-year measurements of ambient ammonia and its relationships with other trace gases at an urban site of Delhi, India, *Meteorol. Atmos. Phys.*, 130, 241–257, <https://doi.org/10.1007/s00703-017-0512-2>, 2018.
- Saylor, R. D., Edgerton, E. S., Hartsell, B. E., Baumann, K., and Hansen, D. A.: Continuous gaseous and total ammonia measurements from the southeastern aerosol research and characterization (SEARCH) study, *Atmos. Environ.*, 44, 4994–5004, <https://doi.org/10.1016/j.atmosenv.2010.07.055>, 2010.
- 605 Schjoerring, J. K., Husted, S., and Mattsson, M.: Physiological parameters controlling plant–atmosphere ammonia exchange, *Atmos. Environ.*, 32, 491–498, [https://doi.org/10.1016/S1352-2310\(97\)00006-X](https://doi.org/10.1016/S1352-2310(97)00006-X), 1998.
- Sheng, M., Zhou, R., Hua, J., Han, S., Liu, S., Zhang, L., Wang, W., Dang, R., Cao, H., Chen, Z., Gu, Y., Liu, M., Lee, L., Qi, C., Lu, F., Han, C., Shephard, M. W., Guendouz, N., Viatte, C., Clarisse, L., Van Damme, M., Clerbaux, C., and Zeng, Z.-C.: Geostationary observations of atmospheric ammonia over East Asia: spatio-temporal variations revealed by three years of FY-4B/GIIRS measurements, *Atmos. Chem. Phys.*, 26, 7803–7826, <https://doi.org/10.5194/acp-26-7803-2026>, 2026.
- 610 Shephard, M. W. and Cady-Pereira, K. E.: Cross-track Infrared Sounder (CrIS) satellite observations of tropospheric ammonia, *Atmos. Meas. Tech.*, 8, 1323–1336, <https://doi.org/10.5194/amt-8-1323-2015>, 2015.
- Shephard, M. W., Cady-Pereira, K. E., Luo, M., Henze, D. K., Pinder, R. W., Walker, J. T., Rinsland, C. P., Bash, J. O., Zhu, L., Payne, V. H., and Clarisse, L.: TES ammonia retrieval strategy and global observations of the spatial and seasonal variability of ammonia, *Atmos. Chem. Phys.*, 11, 10743–10763, <https://doi.org/10.5194/acp-11-10743-2011>, 2011.
- 615 Shephard, M. W., Dammers, E., Cady-Pereira, K. E., Kharol, S. K., Thompson, J., Gainariu-Matz, Y., Zhang, J., McLinden, C. A., Kovachik, A., Moran, M., Bittman, S., Sioris, C. E., Griffin, D., Alvarado, M. J., Lonsdale, C., Savic-Jovicic, V., and Zheng, Q.: Ammonia measurements from space with the Cross-track Infrared Sounder: characteristics and applications, *Atmos. Chem. Phys.*, 20, 2277–2302, <https://doi.org/10.5194/acp-20-2277-2020>, 2020.
- 620 Someya, Y., Imasu, R., Shiomi, K., and Saitoh, N.: Atmospheric ammonia retrieval from the TANSO-FTS/GOSAT thermal infrared sounder, *Atmos. Meas. Tech.*, 13, 309–321, <https://doi.org/10.5194/amt-13-309-2020>, 2020.
- Sutton, M. A., Reis, S., Riddick, S. N., Dragosits, U., Nemitz, E., Theobald, M. R., Tang, Y. S., Braban, C. F., Vieno, M., Dore, A. J., Mitchell, R. F., Wanless, S., Daunt, F., Fowler, D., Blackall, T. D., Milford, C., Flechard, C. R., Loubet, B., Massad, R., Cellier, P., Personne, E., Coheur, P. F., Clarisse, L., Van Damme, M., Ngadi, Y., Clerbaux, C., Skjøth, C. A., Geels, C., Hertel, O., Wichink Kruit, R. J., Pinder, R. W., Bash, J. O., Walker, J. T., Simpson, D., Horváth, L., Misselbrook, T. H., Bleeker, A., Dentener, F., and De Vries, W.: Towards a climate-dependent paradigm of ammonia emission and deposition, *Philos. Trans. R. Soc. B Biol. Sci.*, 368, 20130166, <https://doi.org/10.1098/rstb.2013.0166>, 2013.
- Tevlin, A. G., Li, Y., Collett, J. L., McDuffie, E. E., Fischer, E. V., and Murphy, J. G.: Tall Tower Vertical Profiles and Diurnal Trends of Ammonia in the Colorado Front Range, *J. Geophys. Res.-Atmos.*, 122, <https://doi.org/10.1002/2017JD026534>, 2017.
- 630 Van Damme, M., Erisman, J. W., Clarisse, L., Dammers, E., Whitburn, S., Clerbaux, C., Dolman, A. J., and Coheur, P.-F.: Worldwide spatiotemporal atmospheric ammonia (NH<sub>3</sub>) columns variability revealed by satellite, *Geophys. Res. Lett.*, 42, 8660–8668, <https://doi.org/10.1002/2015GL065496>, 2015.

- Walker, J. T., Robarge, W. P., Wu, Y., and Meyers, T. P.: Measurement of bi-directional ammonia fluxes over soybean using the modified Bowen-ratio technique, *Agric. For. Meteorol.*, 138, 54–68, <https://doi.org/10.1016/j.agrformet.2006.03.011>, 2006.
- 635
- Wang, Q., Zhang, Q., Ma, Z., Ge, B., Xie, C., Zhou, W., Zhao, J., Xu, W., Du, W., Fu, P., Lee, J., Nemitz, E., Cowan, N., Mullinger, N., Cheng, X., Zhou, L., Yue, S., Wang, Z., and Sun, Y.: Temporal characteristics and vertical distribution of atmospheric ammonia and ammonium in winter in Beijing, *Sci. Total Environ.*, 681, 226–234, <https://doi.org/10.1016/j.scitotenv.2019.05.137>, 2019.
- 640
- Wang, T., Song, Y., Xu, Z., Liu, M., Xu, T., Liao, W., Yin, L., Cai, X., Kang, L., Zhang, H., and Zhu, T.: Why is the Indo-Gangetic Plain the region with the largest NH<sub>3</sub> column in the globe during pre-monsoon and monsoon seasons?, *Atmos. Chem. Phys.*, 20, 8727–8736, <https://doi.org/10.5194/acp-20-8727-2020>, 2020.
- Wang, W., Liu, C., Clarisse, L., Van Damme, M., Coheur, P.-F., Xie, Y., Shan, C., Hu, Q., Sun, Y., and Jones, N.: Ground-based measurements of atmospheric NH<sub>3</sub> by Fourier transform infrared spectrometry at Hefei and comparisons with IASI data, *Atmos. Environ.*, 287, 119256, <https://doi.org/10.1016/j.atmosenv.2022.119256>, 2022.
- 645
- Warner, J. X., Wei, Z., Strow, L. L., Dickerson, R. R., and Nowak, J. B.: The global tropospheric ammonia distribution as seen in the 13-year AIRS measurement record, *Atmos. Chem. Phys.*, 16, 5467–5479, <https://doi.org/10.5194/acp-16-5467-2016>, 2016.
- Warner, J. X., Dickerson, R. R., Wei, Z., Strow, L. L., Wang, Y., and Liang, Q.: Increased atmospheric ammonia over the world's major agricultural areas detected from space, *Geophys. Res. Lett.*, 44, 2875–2884, <https://doi.org/10.1002/2016GL072305>, 2017.
- 650
- Weber, R. J., Guo, H., Russell, A. G., and Nenes, A.: High aerosol acidity despite declining atmospheric sulfate concentrations over the past 15 years, *Nat. Geosci.*, 9, 282–285, <https://doi.org/10.1038/ngeo2665>, 2016.
- Wells, K. C., Millet, D. B., Payne, V. H., Deventer, M. J., Bates, K. H., De Gouw, J. A., Graus, M., Warneke, C., Wisthaler, A., and Fuentes, J. D.: Satellite isoprene retrievals constrain emissions and atmospheric oxidation, *Nature*, 585, 225–233, <https://doi.org/10.1038/s41586-020-2664-3>, 2020.
- 655
- Wells, K. C., Millet, D. B., Payne, V. H., Vigouroux, C., Aquino, C. A. B., De Mazière, M., De Gouw, J. A., Graus, M., Kurosu, T., Warneke, C., and Wisthaler, A.: Next-Generation Isoprene Measurements From Space: Detecting Daily Variability at High Resolution, *J. Geophys. Res.-Atmos.*, 127, e2021JD036181, <https://doi.org/10.1029/2021JD036181>, 2022.
- 660
- Zavvalov, V., Esplin, M., Scott, D., Esplin, B., Bingham, G., Hoffman, E., Lietzke, C., Predina, J., Frain, R., Suwinski, L., Han, Y., Major, C., Graham, B., and Phillips, L.: Noise performance of the CrIS instrument, *J. Geophys. Res.-Atmos.*, 118, <https://doi.org/10.1002/2013JD020457>, 2013.
- Zeng, Z.-C.: Global carbon monoxide retrieval from the hyperspectral infrared atmospheric sounder-II onboard FengYun-3E in a dawn-dusk sun-synchronous orbit, *J. Quant. Spectrosc. Radiat. Transf.*, 333, 109336, <https://doi.org/10.1016/j.jqsrt.2024.109336>, 2025.
- 665
- Zeng, Z.-C., Lee, L., Qi, C., Clarisse, L., and Van Damme, M.: Optimal estimation retrieval of tropospheric ammonia from the Geostationary Interferometric Infrared Sounder on board FengYun-4B, *Atmos. Meas. Tech.*, 16, 3693–3713, <https://doi.org/10.5194/amt-16-3693-2023>, 2023.

- 670 Zeng, Z.-C., Clarisse, L., Franco, B., Clerbaux, C., Theys, N., Qi, C., Lee, L., Zhu, L., Hu, X., Gu, M., and Zhang, P.: Volcanic sulfur dioxide monitored from a constellation of FengYun hyperspectral infrared sounders in dawn-dusk, mid-morning, and afternoon sun-synchronous orbits, *Remote Sens. Environ.*, 331, 115057, <https://doi.org/10.1016/j.rse.2025.115057>, 2025.
- Zhan, X., Adalibieke, W., Cui, X., Winiwarter, W., Reis, S., Zhang, L., Bai, Z., Wang, Q., Huang, W., and Zhou, F.: Improved Estimates of Ammonia Emissions from Global Croplands, *Environ. Sci. Technol.*, 55, 1329–1338, <https://doi.org/10.1021/acs.est.0c05149>, 2021.
- 675 Zhang, C., Qi, C., Yang, T., Gu, M., Zhang, P., Lee, L., Xie, M., and Hu, X.: Evaluation of FY-3E/HIRAS-II Radiometric Calibration Accuracy Based on OMB Analysis, *Remote Sens.*, 14, 3222, <https://doi.org/10.3390/rs14133222>, 2022a.
- Zhang, L., Chen, Y., Zhao, Y., Henze, D. K., Zhu, L., Song, Y., Paulot, F., Liu, X., Pan, Y., Lin, Y., and Huang, B.: Agricultural ammonia emissions in China: reconciling bottom-up and top-down estimates, *Atmos. Chem. Phys.*, 18, 339–355, <https://doi.org/10.5194/acp-18-339-2018>, 2018.
- 680 Zhang, P., Hu, X., Lu, Q., Zhu, A., Lin, M., Sun, L., Chen, L., and Xu, N.: FY-3E: The First Operational Meteorological Satellite Mission in an Early Morning Orbit, *Adv. Atmos. Sci.*, 39, 1–8, <https://doi.org/10.1007/s00376-021-1304-7>, 2022b.
- Zhang, P., Hu, X., Sun, L., Xu, N., Chen, L., Zhu, A., Lin, M., Lu, Q., Yang, Z., Yang, J., and Wang, J.: The On-Orbit Performance of FY-3E in an Early Morning Orbit, *Bull. Am. Meteorol. Soc.*, 105, E144–E175, <https://doi.org/10.1175/BAMS-D-22-0045.1>, 2024.
- 685 Zhang, Y., Dore, A. J., Ma, L., Liu, X. J., Ma, W. Q., Cape, J. N., and Zhang, F. S.: Agricultural ammonia emissions inventory and spatial distribution in the North China Plain, *Environ. Pollut.*, 158, 490–501, <https://doi.org/10.1016/j.envpol.2009.08.033>, 2010.
- Zhou, M., Deng, Z., Robert, C., Zhang, X., Zhang, L., Wang, Y., Qi, C., Wang, P., and Mazière, M. D.: The First Global Map of Atmospheric Ammonia (NH<sub>3</sub>) as Observed by the HIRAS/FY-3D Satellite, *Adv. Atmos. Sci.*, 41, 379–390, <https://doi.org/10.1007/s00376-023-3059-9>, 2024.
- 690